Actin polymerization by WASp limits nuclear envelope rupture and inflammation in macrophages

Roberto Amadio[1,2], Giulia Bracchetti[1], Zahraa Alraies[3,#], Giulia Maria Piperno[1], Lucia Lopez Rodriguez[1], Mathieu Maurin[3], Martina Conti[4], Laura Andolfi[4], Maria Carmina Castiello[5,6], Francesca Ferrua[5], Anna Villa[5,6], Alessandro Aiuti[5], Ana-Maria Lennon-Dumenil[3] and Federica Benvenuti[1,*]

[1]Cellular Immunology, International Centre for Genetic Engineering and Biotechnology (ICGEB), Trieste, Italy

[2]University of Trieste, Department of Life Sciences (DSV), 34127 Trieste, Italy

[3]INSERM-U932 Immunité et Cancer, Institut Curie, PLS Research University, 75005 Paris, France

[4]Istituto Officina dei Materiali - National Research Council (CNR-IOM) - Basovizza, Trieste, Italy

[5]San Raffaele Telethon Institute for Gene Therapy (SR-TIGET), IRCSS San Raffaele Scientific Institute, 20132 Milan, Italy

[6]Institute for Biomedical Technologies - National Research Council (CNR-ITB), 20054 Segrate, Milan, Italy

[#]Present address: Laboratory of Cell and Molecular Biology, Experimental Research (C1), 005E - NYU Abu Dhabi, Saadiyat Campus, Abu Dhabi, United Arab Emirates

*Corresponding author, Federica Benvenuti, benvenut@icgeb.org

Abstract

Mutations in the immune-specific actin regulator WASp induce a proinflammatory state in myeloid cells, whose underlying causes remain poorly defined. Here, we applied microfabricated tools that mimic tissue mechanical forces to explore the role of WASp in connecting mechano-sensing to the activation of inflammatory responses in macrophages. We show that WASp-deficient macrophages carry nuclear structure alterations and undergo increased blebbing and nuclear rupture when exposed to mechanical confinement. High-resolution imaging indicates that WASp drives the formation of protective perinuclear actin structures in response to confinement. Functionally, WASp null macrophages respond to mechanical confinement by inducing a transcriptional profile consistent with the release of immunogenic DNA in the cytosol. The proinflammatory state of mechanically confined WASp-deficient macrophages depends, in part, on the cGAS-STING pathway of cytosolic DNA sensing. Together, these data uncover a WASp-dependent mechanism to restrict activation of inflammatory signalling in tissue macrophages and provide hints to target unabated inflammation in Wiskott-Aldrich Syndrome.

Running title: Branched actin polymerization in control of nuclear integrity and inflammation

Keywords: Wiskott-Aldrich Syndrome, actin, nuclear mechanics, nuclear rupture, inflammation

ORCIDs and e-mails:
R.A: 0000-0003-0861-0703, roberto.amadio@icgeb.org

Introduction

Misplaced cytosolic DNA is emerging as a critical cause of inflammation in various monogenic and systemic autoimmune diseases (Decout et al., 2021). Mitochondrial DNA is a well-established immunogenic trigger, engaging TLR9, cGAS or NLRP3, depending on the context (Rodríguez-Nuevo et al., 2018; Maekawa et al., 2019; Xian et al., 2022). In addition, nuclear alterations and genomic DNA damage leads to chromosomal DNA extrusion into the cytosol (Härtlova et al., 2015; Dou et al., 2017; Dunphy et al., 2018). DNA molecules that access the cytosol are detected by sensors such as cGAS and STING and trigger activation of cytokine genes, senescence or cell death, depending on the severity of damage (Dou et al., 2017; Mu et al., 2020; Sladitschek-Martens et al., 2022). Hence, maintaining nuclear integrity is critical to restrict unwanted activation, a process that is particularly relevant in cells that navigate complex environments (Denais et al., 2016), or are continuously exposed to mechanical compression (De Silva et al., 2023). Nuclear stability relies on chromatin mechanics (Nava et al., 2020) and cytoskeletal forces. Within cytoskeletal components, microtubules limit nuclear deformations in dendritic cells (Thiam et al., 2016), while intermediate filaments protect nuclei of murine embryonic fibroblast during constricted migration (Patteson et al., 2019). Arp2/3-dependent branched actin polymerization deforms the nuclei of migrating dendritic cells (Thiam et al., 2016) and maintains nuclear integrity in stromal cells (Sladitschek-Martens et al., 2022). Recently, genetic ablation of the Cdc42 GTPase DOCK8 showed that branched actin polymerization preserves nuclear integrity in T and dendritic cells during confined migration (Reis-rodrigues et al., 2024; Shen et al., 2024), suggesting broader nuclear defects in actinopathies.

The Wiskott-Aldrich Syndrome (WAS) is a primary immunodeficiency characterized by frequent autoimmune and autoinflammatory manifestations. WAS is caused by mutations in Wiskott-Aldrich Syndrome protein (WASp), a critical activator of the Arp2/3 complex which controls branched actin polymerization specifically in non-erythroid immune cells (Blundell et al., 2010; Naseem et al., 2022). Altered platelets generation, autoreactive B cells and impaired Tregs function predispose to autoimmunity in Wiskott-Aldrich Syndrome (WAS) (Sereni et al., 2018; Calixto Vieira et al., 2023). Our group identified a link between the release of immunogenic DNA by neutrophil extracellular traps and excessive production of type-I interferon by WASp KO (WKO) plasmacytoid dendritic cells (pDCs) (Prete et al., 2013; Cervantes-Luevano et al., 2018). In addition, WKO macrophages activates the inflammasome due to impaired bacterial clearance (Lee et al., 2017), and defective maturation of the endolysosomal network upon engulfment of circulating immuno-complexes triggers TLR9 and cGAS pathways in DCs (Piperno et al., 2020; Amadio et al., 2021). WASp has been observed to

polymerize actin patches in dendritic cells migrating inside confined environments, which push perpendicularly to the direction of movement and maintain vertical space for the cell to crawl (Gaertner et al., 2022). Despite these observations, a direct contribution of WASp to nuclear stability and inflammation in myeloid cells remains elusive.

In this work, we studied the role of WASp in preserving nuclear stability under mechanical pressure. By combining microfabricated tools that mimic tissues' mechanical forces, imaging and transcriptional profiling, we found that WASp-driven actin polymerization contributes to nuclear envelope integrity and counteracts mechanical challenge in macrophages. Consequently, lack of WASp causes inflammatory activation by extruded genomic DNA, which is in part mediated by STING.

Results

Inflammatory phenotype in mouse and human WKO macrophages

Macrophages are the most abundant myeloid cells subset in tissues and critically contribute to inflammation in pathological conditions (Ginhoux and Guilliams, 2016). WASp null macrophages were recently shown to express an inflammatory signature at steady state (Liang et al., 2023). To investigate whether mechanical compression further induces inflammation in WKO macrophages, we focused on lung alveolar macrophages (AMO), a representative population of long-lasting resident macrophages constantly exposed to physical constrains and subjected to almost 2D confinements (De Silva et al., 2023). Flow cytometry profiling of AMO (Supplementary Fig.1A), showed higher levels of the activation marker CD86 in WKO mice (10 weeks of age), as compared to WT (Fig.1A). We next isolated AMO from 10 weeks and 25 weeks old mice. The absolute number of AMO was higher in WKO as compared to controls, especially at 25 weeks of age (Fig.1B). Notably, two key inflammatory genes were significantly induced in AMO from 25 weeks old WKO mice (Fig.1C). Similarly, bone marrow-derived macrophages expressed higher activation of inflammatory genes (Fig.1D). We conclude that, consistently with previous findings in the spleen (Prete et al., 2013; Liang et al., 2023), WASp deficient macrophages are constitutively activated and that this phenotype is exacerbated by tissue residency *in-vivo*.

To translate the importance of macrophage activation to humans, we designed an inflammatory signature (Supplementary Table 1) and used it to interrogate two different data sets. First, we re-analysed a publicly available dataset of WKO iPSCs-derived macrophages (GSE107963, TPM normalized reads), and their isogenic counterparts that have been corrected to re-express WASp (Yuan et al., 2022). The inflammatory score, as well as relevant inflammatory genes, were consistently reduced by restoring WASp expression in iPSCs (Fig.1E and F). We then performed a bulk RNA-seq on a cohort of PBMCs from 6 WAS patients, before and after WASp reconstitution by gene therapy. Major WAS defects (i.e. BCR signalling and genes related to platelets function) were normalized upon re-expression of WASp, without inducing alteration in other Arp2/3 activators (Supplementary Fig.1B and C). Interestingly, despite the complex composition of PBMCs that comprises several subsets (mainly B, T, NK and monocytes) and patient heterogeneity, we found higher inflammation in WAS samples, which was diminished by WASp restoration (Fig.1G and H). Selected inflammatory genes emerging from RNA-seq, were validated by RT-qPCR, confirming that

159 re-introducing WASp is sufficient to normalize expression to the level of healthy donors
160 (Supplementary Fig.1D). Intriguingly, the overall correction index was greater in samples showing a
161 higher basal level of inflammation (Supplementary Fig.1E). Altogether, our data indicate that WASp
162 restrain expression of inflammatory genes in mouse macrophages and human cells.
163
164 **Nuclear defects in WKO macrophages**
165 Having established that WASp deficiency correlates with elevated expression of inflammatory genes,
166 we next sought to explore the underlying molecular basis. For this purpose, we moved to bone
167 marrow-derived macrophages (BMDM) that recapitulate inflammatory features and are easy to
168 obtain in large numbers. We initially assessed simple nuclear parameters in 2D, such as area,
169 roundness and micronuclear occurrence (Fig.2A). We found that the nuclei of WKO macrophages
170 had an increased mean projected area, were more irregular and showed a higher incidence of
171 micronuclei (Fig.2B), indicating general alterations in nuclear homeostasis. Previous findings in other
172 systems linked defects in Lmna (encoding for Lamin A/C) and nuclear envelope folding to impaired
173 mechanical tension and reduced protection from deformations (Kim et al., 2017; Tang et al., 2023).
174 We thus focused on Lamin A/C and the nuclear envelope protein Emerin in our model. Total Lamin
175 A/C levels were reduced in WKO, both at the mRNA and protein level, whereas mRNA expression of
176 type B lamins and Emerin were not different (Fig.2C and D). Importantly, we noticed higher degree
177 of Lamin A/C wrinkles and irregularities in nuclei of WASp null macrophages (Fig.2E), which
178 coincided with Emerin accumulation (Fig.2F). Altogether these data suggest defective nuclear
179 envelope homeostasis and increased folding of the nuclear envelope in the absence of WASp.
180 Next, as the nucleus is highly connected to chromatin and cellular mechanics, we explored chromatin
181 parameters and global cellular stiffness. We did not observe substantial differences in global
182 heterochromatin content and peripheral heterochromatin between the two genotypes by
183 chromocenters analysis (Supplemental Fig.2A). Similarly, no changes in heterochromatin distribution
184 were detected by H3K9me2 staining, but an increase in the total intensity of this marker
185 (Supplemental Fig.2B). Cellular mechanics, as measured by Atomic Force Microscopy (AFM)
186 indentation (Supplementary Fig.2C) showed that WKO cells were stiffer than WT ones
187 (Supplementary Fig.2D). Of note, a stiffer cytoplasm has been linked to reduced nuclear stability
188 under 3D physical constrains (Bastianello et al., 2023). Together, these initial data indicate a global
189 defect in nuclear-cytoskeletal mechanics in macrophages derived from WASp null animals, which
190 may affect nuclear stability under 3D tissues forces.

191 **Increased constricted migration and nuclear deformation in WKO macrophages**

192 To test the hypothesis of reduced nuclear stability in WKO, we first used an assay to measure nuclear
193 deformations in macrophages inside narrow constrictions by means of microchannels (Vargas et al.,
194 2016). We adopted different channel dimensions, ranging from 2 µm to 8 µm in width and having a
195 constant height of 5 µm. Macrophages were seeded in the pre-channel chamber and recorded
196 overnight. The number of cells that entered the channel was calculated at the end of the recording
197 period by counting the number of cells inside channels and normalizing by the number of
198 approaching cells (Supplementary Fig.3A; materials and methods). As expected, reducing the size of
199 the channel, limited the number of cells entering inside constrictions (Fig.3A). Interestingly, the
200 entrance rate of WKO macrophages was consistently higher, especially at smaller constrictions
201 (Fig.3B). By carefully inspecting nuclear shape in cells inside channels we observed an increased rate
202 of nuclear herniations in WKO (Fig.3C). The ratio between front and back herniations was not
203 different between genotypes and skewed to the front (Fig.3D), as already expected based on
204 observations in other cell types (Denais et al., 2016). Since herniations predispose to nuclear
205 rupture, we next transduced BMDM with a lentiviral construct expressing nuclear localization signal
206 (NLS)-tagged GFP (NLS–GFP), which is retained inside nuclei and released only upon nuclear
207 envelope break (Fig.3E). Interestingly, we observed a larger fraction of WKO macrophages
208 undergoing nuclear envelope (NE) rupture and cytosolic release of fluorescent signal than WT (Fig.3F
209 and G). Moreover, and consistent with increased nuclear fragility, we detected multiple rupture
210 events on the same cell exclusively in WKO (Fig.3H).

211

212 A parallel set of experiments confirmed the superior ability of WASp null cells to translocate through
213 small pores in transwell assays (Supplementary Fig.3B). Notably, migration induced an increase in
214 nuclear deformation as well as γH2AX staining, particularly in WKO cells (Supplementary Fig.3C).
215 Expression of the relevant chemokine receptor targeted to promote transmigration was equal in the
216 two genotypes, ruling out that defective sensing of the chemotactic gradient affected the observed
217 migration rate (Supplementary Fig.3D). Overall, these data indicate that WASp-deficient
218 macrophages have an enhanced ability to navigate through small constriction, in line with a previous
219 report on dendritic cells (Gaertner et al., 2022), suggesting reduced resistance to nuclear
220 deformation. Importantly, the nuclear envelope of WKO cells ruptures during constricted migration,
221 releasing nuclear material into the cytosol.

222

223 **WASp limits nuclear ruptures under mechanical confinement**

224 To more faithfully recapitulate deformation events experienced by macrophages in tissues, we next
225 applied a vertical confiner device (Alraies et al., 2024) based on PDMS micropillars (Supplementary
226 Fig.4A). The heights of BMDM nuclei plated on fibronectin-coated glass slides without confinement
227 range between 5 and 6 µm (Supplementary Fig.4B), therefore we selected a height of 6 µm and 3
228 µm as mild and strong confinement respectively (Supplementary Fig.4C). Confocal images were
229 acquired after one hour of confinement to examine nuclear parameters. We classified nuclei into
230 two categories: 1) intact, when the nuclear boundaries were regular and continuous; 2) damaged,
231 when blebs or herniations were found to interrupt the nuclear perimeter. (Fig.4A). The fraction of
232 damaged nuclei in WASp null cells was slightly higher under mild confinement and significantly
233 higher under strong confinement (Fig.4B), suggesting loss of nuclear integrity. Indeed, measuring
234 NLS-GFP localization after confinement at 3 µm, we observed an increased frequency of NE rupture
235 and NLS-GFP cytosolic release in WKO cells (Fig.4C and D). Live tracking of NLS-GFP leakage revealed
236 that this event was often preceded by blebbing/herniation of the nuclear surface (Fig.4E). To causally
237 link WASp to nuclear deformation and loss of NE integrity, we next transduced WASp null
238 macrophages with a lentiviral construct expressing WASp-GFP (Supplementary Fig.4D) (Blundell et
239 al., 2008). This resulted in around 50% of cells expressing a clear GFP signal and WASp-GFP fusion
240 protein of the expected size (Supplementary Fig. 4E and F). The resulting mixed population of GFP-
241 positive (rescued) and negative (control) cells was subjected to confinement at 3 µm. In this highly
242 controlled setting, we found that GFP-positive cells showed significantly fewer nuclear blebs than
243 GFP-negative ones (Fig. 4F and G). Moreover, the fraction of cells showing Lamin A/C rupture was
244 reduced in WASp-GFP positive cells (Fig.4H and I), confirming a direct impact of WASp in preserving
245 nuclear stability under confinement.

246

247 **WASp directs perinuclear actin polymerization in confined macrophages**

248 We then aimed to investigate a potential mechanism by which WASp and actin polymerization
249 support nuclear stability during mechanical challenge. We took advantage of a fixation-under-
250 confinement protocol, which maintains intact cytoskeletal structures once confinement is released
251 (Alraies et al., 2024). Accumulation of dense actin structures in the central body of the cell were
252 induced by confinement in WT but not in WKO macrophages (Fig.5A). These actin patches closely
253 resemble the Arp2/3-dependent structures described in mechanically confined dendritic cells with
254 a role in nuclear envelope unfolding (Alraies et al., 2024). By high-resolution imaging, we further

255 classified confined cells into four categories according to actin distribution: 1) perinuclear actin
256 patches; 2) intranuclear actin accumulation; 3) filamentous perinuclear actin ring and 4) diffuse
257 cytosolic actin (Fig.5B). Among central body actin structures, perinuclear actin patches were
258 observed in a substantial proportion of WT cells but were virtually absent in WKO cells (Fig.5C and
259 D). Intranuclear actin accumulation was present in a small fraction of cells, in similar frequencies
260 between the two genotypes. Additionally, a small fraction of WKO cells showed thin filamentous
261 actin surrounding the nucleus (Fig.5C and D), a phenomenon not detected in WT. To explore the role
262 of WASp in driving the polymerization of perinuclear actin structures, we leveraged WKO
263 macrophages transduced with WASp-GFP for colocalization analysis (Fig.5E). Of note, the Mander's
264 coefficient between phalloidin and GFP was high in the perinuclear actin patches induced by
265 confinement (Fig.5F), strongly suggesting an active role of WASp in directing the formation of these
266 structures. Consistently, also the distribution of WASp-GFP in macrophages inside microchannels
267 was enriched in the central part of the cell body and around the nucleus (Supplementary Fig.5A and
268 B). We conclude that WASp drives the nucleation of perinuclear actin patches in macrophages
269 exposed to mechanical confinement. Together with the previous observations, this result suggests
270 that a local perinuclear actin response may help to preserve nuclear integrity.
271
272 **Confinement-induced nuclear ruptures exacerbate inflammation in WKO macrophages**
273 To investigate the functional consequences of increased nuclear fragility in WKO, we analysed the
274 transcriptional profiles of macrophages upon confinement (Fig.6A). WT and WKO macrophages at
275 steady state (unconfined) express a common transcriptional program and some genotype-specific
276 genes (Supplementary Fig.6A). Remarkably, WKO cells were enriched in immunoglobulin coding
277 genes, an observation that deserves future investigations. Moreover, transcripts related to
278 extracellular matrix organization, vascular remodelling and cellular activation/migration were higher
279 in unconfined WKO macrophages than in WT. In contrast, genes controlling cellular metabolism were
280 less expressed in WKO (Supplementary Fig.6A and Supplementary Table 2). Confinement induced
281 profound transcriptional remodelling in both genotypes (Supplementary Fig.6B). Analysis of
282 differentially expressed genes (DEGs) between unconfined and confined cells unveiled a core of
283 upregulated genes shared by WT and WKO (Fig.6B), including some inflammatory cytokines and
284 chemokines (Fig.6C). Interestingly, we observed several genes controlling cell activation and tissue
285 remodelling selectively upregulated in confined WKO cells (Fig.6B), paralleled by reduced expression
286 of metabolic pathways (Supplementary Fig.6C), indicating increased activation in WASp KO samples.

287 To explore the molecular mechanisms underlying cellular responses to confinement, we evaluated
288 the expression of genes implicated in cytoskeletal dynamics and control of nuclear stability
289 (Supplementary Table 4) across all the conditions. A signature including genes that control actin
290 branching (branched actin score) was significantly higher in WT than in WKO macrophages,
291 suggesting that WASp deficiency broadly impacts the process. Confinement induced transcriptional
292 activation of this set of genes in both genotypes, indicating a fast cellular adaptation to mechanical
293 inputs (Fig.6D). However, expression in WKO remained consistently lower despite a mild induction
294 by confinement. This trend was even more prominent when selecting specific WASp effectors that
295 have been directly linked to NE integrity (*Actr2*, *Actr3*, *Arpc4)* (Sladitschek-Martens et al., 2022;
296 Delgado, 2024); showing a drastic reduction of expression in both unconfined and confined WASp
297 deficient cells. Of note, a second gene module linked to nuclear mechanics including several genes
298 previously implicated in NE stability, such as Lamin A/C, Emerin and Lap2β (Tmpo) (Chen et al., 2021;
299 Lavenus et al., 2022; De Silva et al., 2023) was significantly upregulated in WT cells, but not in WKO,
300 upon confinement (Fig.6E). Conversely, SUN2 and RhoA/ROCK, whose overexpression has been
301 linked to nuclear blebbing and innate activation (Mu et al., 2020), were much more induced in WKO,
302 together with RAC2-related genes (Supplementary Fig.6D). All together, these data suggest a
303 defective branched actin-based response to confinement in WKO macrophages, concomitant to
304 induction of a compensatory RhoA/RAC-mediated pathway, with a potentially negative impact on
305 nuclear stability.
306
307 Defective mechanotransduction and reduction in the expression of genes linked to actin-dependent
308 nuclear integrity were previously shown to induce activation of a proinflammatory cell state in
309 Arp2/3 deficient fibroblast (Sladitschek-Martens et al., 2022). Hence, we examined the expression
310 of this signature, defined as "nuclear envelope rupture (NER) inflammatory score" in our dataset.
311 Remarkably, the NER inflammatory score was selectively activated in confined WASp null
312 macrophages, causally connecting WASp to the control of proinflammatory activation in cells
313 exposed to mechanical inputs (Fig.6F). Among the genes included in NER inflammatory score, Il6 was
314 selected to perform further functional analyses. qPCR confirmed that Il6 transcripts are
315 preferentially induced by confinement in WKO (Fig.6G). To exclude any potential bias in macrophages
316 derived from constitutive WASp KO animals, we induced acute WASp deletion in WT BMDM by
317 CRISPR-Cas9 gene editing (Supplementary Fig.6E). Importantly, WASp-depleted macrophages
318 responded to confinement by augmented Il6 induction as compared to control cells (Fig.6H),

319 indicating that WASp directly restricts confinement-induced activation. Given the widespread
320 implications of the cGAS-STING pathway of cytosolic DNA sensing (Ablasser and Gulen, 2016) to
321 innate activation and specifically in driving the NER inflammatory score (Sladitschek-Martens et al.,
322 2022), we assessed its contribution to confinement-induced activation of WKO cells. Efficient STING
323 ablation in WKO macrophages (Supplementary Fig.6F) blunted Il6 production upon direct
324 stimulation by DMXAA, confirming the functional disruption of the pathway (Supplementary Fig.6D).
325 We then exposed WKO macrophages carrying or not STING depletion to confinement at 3 µm of
326 height. Induction of Il6 transcripts was significantly reduced in WKO STING KO macrophages as
327 compared to STING-proficient cells, causally connecting the pathway to the proinflammatory state
328 of WKO macrophages (Fig.6I). The partial ablation of Il6 responses in STING-depleted cells, suggests
329 that other sensors/mechanisms contribute to the inflammatory activation downstream of NE
330 ruptures in WASp-deficient cells.
331 Collectively, these data uncover a differential transcriptional response by WASp null macrophages to
332 mechanical confinement, showing that WASp limits NE ruptures and the firing of cytokine signalling
333 in myeloid cells exposed to physiologically relevant constrains (Fig.6J).
334
335
336
337
338
339
340
341
342
343
344
345
346
347
348
349
350

Discussion

In this study we identified an unprecedented role for WASp in preserving nuclear integrity, thus restraining inflammatory responses in macrophages exposed to tissue forces.

The direct connection between WASp-mediated actin polymerization and nuclear integrity has emerged by studying macrophages in confined environments that recapitulate tissue forces experienced *in-vivo*. Hence, the approach used in this study uncovers an essential supplementary function for the hematopoietic-specific actin nucleation-promoting factors WASp, beyond the well-established role at the cell cortex and in intracellular trafficking (Linder et al., 1999; Piperno et al., 2020; Gaertner et al., 2022). These findings are particularly relevant given the intrinsically migratory nature of immune cells and the nucleus as the main rate-limiting factor for constricted migration.

Previous studies showed that WASp null dendritic cells migrate faster inside microchannels or through constriction. However, the findings were not interpreted as dependent on altered nuclear properties (Gaertner et al., 2022; Oliveira et al., 2022). Our analysis confirms that WASp null macrophages, likewise dendritic cells, are facilitated in entering small constrictions. Additionally, we show that this phenomenon is linked to the enhanced ability of the nucleus to deform and a predisposition to undergo nuclear rupture. Cells harbouring defects in Lamin A/C or a disrupted nuclear-cytoskeleton coupling show similar nuclear deformations, increased migration and high rates of nuclear ruptures when exposed to mechanical confinement (Davidson et al., 2014; Harada et al., 2014; Kim et al., 2017; Bell et al., 2022). In line with our findings, a parallel study by our collaborators observed increased nuclear deformation and ruptures in confined dendritic cells that lack the WASp effector Arp2/3 (Delgado, 2024). More than one mechanism, not mutually exclusive, may explain reduced nuclear integrity in WASp null cells. The dense F-actin patches formed upon confinement and the immediate transcriptional response to supply factors controlling actin branching in WT, but not in WKO cells, suggest that WASp induces cytoskeletal remodelling downstream of mechanical stimuli, creating a protective perinuclear actin barrier. Alternatively, as indicated by the thin actin rings surrounding the nucleus in a fraction of WKO cells and by gene expression data, lack of WASp may drive compensatory actin polymerization by different factors. As documented in a previous report, the resulting abnormal actin network may cause rupture by exerting excessive pressure on the NE under confinement (Mu et al., 2020). Interestingly, similar perinuclear actin rings were also observed in epithelial cells upon mechanical stretching, which has a role in promoting chromatin compaction (Le et al., 2016). Moreover, we cannot exclude that WASp

limits nuclear rupture by acting at the DNA level, protecting it from damage (Kovacs et al., 2023), as it occurs in the case of Arpc4 (Delgado et al. 2024). Of note, despite mild Lamin A/C defects and slight accumulation of DNA damage in WASp null macrophages, the number of tissue-resident cells *in-vivo* is not affected, as opposed to the phenotype in Arpc4 and LMNA/C deficient animals where Langerhans cells and alveolar macrophages, respectively, are depleted in tissues (De Silva et al., 2023; Delgado, 2024). Therefore, WASp ablation induces a milder phenotype than complete blockade of Arp2/3 or Lamin A/C deletion, and cells can cope with nuclear damage by inducing inflammation but without undergoing death.

The unscheduled release of genomic DNA into the cytosol has been documented consequently to DNA damage (Dunphy et al., 2018; Mukherjee et al., 2019; Song et al., 2021), defective Lamin A/C (De Silva et al., 2023; En et al., 2024) and disrupted mechano-signalling due to reduced expression of Arp2/3 regulators, a direct WASp effector (Sladitschek-Martens et al., 2022). The latter study associated nuclear instability and rupture to cGAS-STING activation and senescence induction in fibroblast. We observed a similar inflammatory activation downstream of NE rupture in WKO, raising many interesting points. While STING predominantly activates IRF3 upon exogenous introduction of DNA in the cytosol by transfection, leakage of genomic DNA following DNA damage leads to unconventional STING signalling, predominantly engaging NF-kB rather than IRF3 (Dunphy et al., 2018). Our NER inflammatory activation skewed towards cytokines rather than interferon supports the latter mechanism of STING engagement. Importantly, our work does not exclude the potential involvement of other DNA sensors nor the role of additional mechanisms connecting nuclear deformation and rupture to proinflammatory signalling in WASp null cells. Remarkably, the NER inflammatory signature induced in confined WASp null macrophages has been linked to the induction of senescence in fibroblasts (Sladitschek-Martens et al., 2022). Even if we have not explored senescence in WASp null cells or tissues, the expression of this signature under confinement, together with Lamin A/C defects and nuclear rupture, lead us to speculate that lack of WASp may predispose to accelerated ageing of the myeloid compartment *in-vivo*. Beyond the specific role of WASp described here, our findings suggest that general actin defects may be linked to inflammatory conditions due to nuclear alterations, as proposed by others (Sladitschek-Martens et al., 2022), underscoring the relevance of investigating mechanical control of inflammation in immune cells. From a clinical perspective, our study has implications for understanding the molecular basis of WAS autoimmunity. Transcriptional data in human iPSCs-derived macrophages and total cells from the peripheral blood of gene therapy-treated WAS patients consistently indicate

that WASp restricts the accrual of inflammation. However, inflammatory relapses are still frequent after treatment in WAS, including hematopoietic stem cell transplantation (Sudhakar et al., 2021). According to recent evidence, including the data presented here, gene therapy offers better control of inflammation in treated patients (Sereni et al., 2019; Magnani et al., 2022). Nevertheless, defining the precise origin and cellular basis of WAS inflammation is important to designing the management of residual inflammation, especially for those patients who do not have access to gene therapy.

In summary, our results unveil a cell-intrinsic WASP-mediated mechanism to control nuclear stability and inflammation under physiologically relevant settings, expanding the role of WASp-driven Arp2/3 actin polymerization in preserving myeloid cell homeostasis in tissues.

447 # Materials and methods

448

449 ## Reagents and tools table

450

Reagent/Resource	Reference or Source	Identifier
Experimental Models		
WASp$^{-/-}$ mice - B6.129S6-Wastm1Sbs/J	Jackson #:019458	IMSR_JAX:019458
HC and WAS PBMCs	San Raffaele Institute	Supplementary Table 5
Recombinant DNA		
pCDH-NLS-GFP	Addgene	#132772
pMD2.G	Addgene	#12259
psPAX2	Addgene	#12260
SEWW-eGFP-WASp	(Blundell et al., 2008)	/
Antibodies Flow cytometry		
CD45 - APC-Cy7	BioLegend	103114
CD11c - Bv786	BioLegend	117335
F4/80 - Bv421	eBioscience	25-5870-80
MHC-II - AF700R	BioLegend	151507
LY6C - PE	eBioscience	11-0541-81
CD64 - BV605	BioLegend	108923
SiglecF - PerCP-Cy5.5	BioLegend	107105
CD80 - APC	BioLegend	139323
CD86 - Bv650	BioLegend	104713
CD3 - FITC	BioLegend	100305
LY6G - FITC	Bio-Rad	MCA6077GA
B220 - FITC	BioLegend	103208
CD19 - FITC	BioLegend	115503
NK1.1 - FITC	BioLegend	116410
Antibodies FACS		
CD11c - Bv786	BioLegend	117308
SiglecF - PerCP-Cy5.5	BioLegend	121406
Antibodies immunofluorescence		
Anti-Emerin	Thermo Fischer	PA5-29731
Anti-H3K9me2	Abcam	ab1220
Anti-LMNA/C	Cell Signalling	mAb#4777 (4C11)

Anti-γH2AX	Sigma Aldrich	05-636 (JBW301)
Anti-Mouse-488, Donkey	Invitrogen	A21202
Anti-Mouse-555, Goat	Invitrogen	A21424
Anti-Mouse-647, Chicken	Invitrogen	A21463
Anti-Rabbit-488, Goat	Invitrogen	A21441
Anti-Rabbit-594, Donkey	Invitrogen	A21207
Antibodies western blot		
Anti-GAPDH-HRP	Sigma Aldrich	G9295 (GAPDH-71.1)
Anti-WASp	Santa Cruz Biotech	sc-13139 (B-9)
Anti-LMNA/C	Cell Signalling	mAb#4777 (4C11)
Anti-STING	Cell Signalling	13647 (D2P2F)
Anti-TUBα-HRP	Cell Signalling	#9099 (11H10)
Anti-mouse-HRP	Jackson	115-035-003
Anti-Rabbit-HRP	Jackson	711-035-152
Chemicals, Enzymes and other reagents		
2-mercaptoethanol	Gibco	31350010
ACK lysis buffer	Gibco	A1049201
Alexa Fluor™ 555 Phalloidin	Thermo Fischer	A34055
Alt-R® Cas9 Electroporation Enhancer	IDT	1075916
Alt-R® CRISPR-Cas9 tracrRNA	IDT	1072533
Alt-R® Negative Control crRNA #2	IDT	1072545
Alt-R™ crRNA STING	IDT	Mm.Cas9.TMEM173.1.AA
Alt-R™ crRNA WASp	IDT	Mm.Cas9.WAS.1.AC
Alt-R™ spCas9 Nuclease V3	IDT	1081058
Bovine Serum Albumine (BSA)	Sigma Aldrich	A8806
Clarity ECL substrate	Bio-Rad	170-5060
Collagenase type 2	Worthington	LS004176
Counting Bright beads	Miltenyi	C36950
DMXAA	Invivogen	tlrl-dmx
DNAse I from bovine pancreas	Millipore-Sigma	11284932001
EDTA	Thermo Fischer	15575020
FBS - low endotoxin	Euroclone	ECS0186D - lot. EUS037123
Fibronectin Bovine protein	Thermo Fischer	33010-018
Gentamicin	Gibco	15710064
Glycine	Sigma Aldrich	G7126
Hepes	Invitrogen	15630080

Hoechst 33342	Invitrogen	H3570
IMDM medium	Thermo Fischer	31980030
Lenti-X concentrator	Takara	631231
Live and Dead staining –-Bv510	Invitrogen	L34966
LPS	Invivogen	tlrl-pb5lps
Mouse CD11c microbeads	Miltenyi	130-125-835
Mowiol 40-88	Sigma Aldrich	324590
PDMS; SYLGARD 184	Dow	1673921
PFA	Thermo Fischer	28908
Poly-Ethylene-Glycol (PEG)	Sigma Aldrich	81260-1KG
PrimeScript™ RT Reagent Kit	Takara	RR036A
Protein inhibitor cocktail	Sigma Aldrich	P8340
Recombinant mouse CCL19 (MIP3-β)	Gibco - Peprotech	250-27B-1MG
Recombinant mouse MSC-F	Miltenyi	130-101-706
RIPA buffer	/	/
RNA Later™	Invitrogen	AM7021
RPMI 1640 medium	Thermo Fischer	72400047
Sodium Azide	Sigma Aldrich	13412
Sodium pyruvate	Gibco	11360070
Supernatant-containing GM-CSF	Produced by J558 cells	/
TB Green® Premix kit	Takara	RR420A
Triton-X-100	Sigma Aldrich	X100-500ML
TRIzol™ reagent	Thermo Fischer	15596026
Tween-20	Sigma Aldrich	02286
Kits		
BCA assay kit	Thermo Fischer	23225
RNA high-sensitivity kit	Agilent	5067-5579
RNeasy micro kit	Qiagen	74004
Universal Index Twist kit 96	Diatech-Labline	101307
WatchMaker - mRNA Library Prep Kit	Diatech-Labline	7BK0001-024
Software		
Fiji (ImageJ)	v.1.54f	/
FlowJo	Tree Star, Inc. v.10.8.2	/
Graphpad	Prism v.8.0.1	/
R software	R version 4.3.1	/
Other		

J-558 cell line (GM-CSF producers)	/	/

Methods and protocols

Mice

WASp$^{-/-}$ mice (IMSR_JAX:019458) on a C57BL/6 genetic background were a gift from S. Snapper (Massachusetts General Hospital, Boston, Massachusetts, USA) (Snapper et al., 1998). Animal care and experimentation were conducted under national and international laws and policies (Italian D.L.gs. no. 26/2014 art.3.1A; European Directive 63/2010/UE). Mice were bred and maintained at the ICGEB animal Bio-experimentation facility in sterile isolators (12h/12h light/dark cycle, T 21 °C ± 2 °C, RH 55% ± 10%) and received a standard chow diet and water *ad libitum*. Experiments involving *ex-vivo* bone marrow culture were performed using WKO males' mice and WT littermates as controls of 8-12 weeks of age. In case of *in-vivo* experiments WASp$^{-/-}$ and heterozygous WASp$^{+/-}$ female mice of 10 and 25 weeks of age were employed.

Primary murine cell culture and human PBMCs

Mouse BM-derived macrophages (BMDMs) were generated in vitro from BM of C57BL/6 WT or WKO mice using recombinant M-CSF (rMCSF, Miltenyi Biotech). BM-derived cells were cultured at a concentration of 1×10^6 cells/mL in non-treated 10 cm Petri dishes (Greiner) for 7 days using RPMI 1640 supplemented with 20 ng/mL rMCSF, 10% low endotoxin FBS (Euroclone), plus 50 µg/mL gentamicin (Gibco), 50 µM 2-mercaptoethanol (Gibco) and 1% Sodium Pyruvate (Gibco). Mouse BM-derived DCs (BMDCs) were generated in vitro from bone marrow of C57BL/6 WT or WKO mice using supernatant containing GM-CSF produced from J558 cell line. BMDCs were cultured at a concentration of 1.5×10^6 cells/mL in Nunc-nontreated 6 well-plates (Thermo Fisher Scientific) for 7 days using IMDM supplemented with 30% GM-CSF supernatant, 10% low endotoxin FBS (Euroclone), 50 µg/mL gentamicin (Gibco) and 50 µM 2-mercaptoethanol (Gibco). All mice used for BM culture were males of 7 to 12 weeks of age.

Human PBMCs were gently provided by Dr. Anna Villa from San Raffaele Institute and shipped in RNA Later™ (Thermo Fischer Scientific). RNA extraction and library preparation for sequencing are

481 described in the respective paragraphs. Information about patients is provided in supplementary
482 table 5.
483
484 **Flow cytometry and sorting of alveolar macrophages**
485 Alveolar macrophages (AMO) were obtained from homozygous WASp$^{-/-}$ or heterozygous WASp$^{+/-}$
486 female mice of 10 or 25 weeks old. After animal sacrifice, lungs were perfused in PBS to wash away
487 red blood cells and digested with collagenase type 2 (265 U/mL; Worthington) and DNase I
488 (250 U/mL; Millipore-Sigma) in complete media at 37°C for 30'. Collagenase activity was then
489 stopped by EDTA 10 mM, and cell suspension was filtered using 100 µm cell strainer (Corning). The
490 obtained single cell suspension was enriched for CD11c+ population using the mouse CD11c
491 microbeads (Miltenyi) and stained with anti-CD11c, anti-CD45 and anti-SiglecF. 5×10^6 cells/mL were
492 resuspended in PBS 2% FBS for sorting and at least 100.000 AMO were sorted with a BD FACSAria II
493 in PBS 20% FBS. Sorted AMO were centrifuged and frozen at -70°C in 350 µL of RLT lysis buffer prior
494 to RNA extraction. Flow cytometry analysis was performed in a BD FACSCelesta™ starting from 1/5
495 of single cell suspension before CD11c enrichment, using antibodies reported in supplementary
496 table 6 and Counting Bright beads (Miltenyi). All antibodies were incubated 1 h at 4°C in dark
497 conditions. After antibody staining, samples were incubated 20' at 4°C in dark conditions with Live
498 and Dead fixable aqua (Invitrogen) 1:1000 in PBS and fixed over-night in PBS 1% PFA before a final
499 wash and acquisition. Data analysis was performed on FlowJo software.
500
501 **RNA extraction and gene expression analysis**
502 RNA from BMDM at steady state was obtained using of TRIzol™ reagent (Thermo Fischer Scientific)
503 and treated with DNaseI before retro transcription. RNA extraction and purification of sorted AMO,
504 confined BMDM and human PBMCs was performed by RNeasy micro kit (Qiagen). Retro
505 transcription and qPCR were done by PrimeScript™ RT Reagent Kit (Takara) and TB Green® Premix
506 (Takara). Real time machine used for qPCR was a CFX96 Touch (Bio-Rad). Specific primers used for
507 amplification were the following (5'-> 3'):
508
509 <u>Mouse</u>: Gapdh fwd AGAAGGTGGTGAAGCAGGCAT, Gapdh rev CGAAGGTGGAAGAGTGGGAGT; Ifnb1
510 fwd GCACTGGGTGGAATGAGTCT, Ifnb1 rev AGTGGAGAGCAGTTGAGGACA; Il1b fwd
511 TGTAATGAAAGACGGCACACC, Il1b rev TCTTCTTTGGGTATTGCTTGG; Il6 fwd
512 GAGGATACCACTCCCAACAGA, Il6 rev AAGTGCATCATCGTTGTTCAT; Isg15 fwd

513 AGCAATGGCCTGGGACCTAAA, Isg15 rev CAGACCCAGACTGGAAAGGG; Mx1 fwd
514 TCATCAGAGTGCAAGCGAGG, Mx1 rev TCTGATACGGTTTCCTGTGCT; Tnfa fwd
515 CTGTAGCCCACGTCGTAGC, Tnfa rev TTAAGATCCATGCCGTTG.
516
517 Human: Hprt1 fwd AATTATGGACAGGACTGAACGTCTTGCT, rev
518 TCCAGCAGGTCAGCAAAGAATTTATAGC; Mxa fwd ACAGAACCGCCAAGTCCAAA, rev
519 GCGGATCAGCTTCTCACCTT; Rsad2 fwd ATCCTTTGTGCTGCCCCTTG, rev
520 TTGATCTTCTCCATACCAGCTTCC; Il6 fwd AGACAGCCACTCACCTCTTCAG, rev
521 TTCTGCCAGTGCCTCTTTGCTG; Il1b fwd ATGATGGCTTATTACAGTGGCAA, rev
522 GTCGGAGATTCGTAGCTGGA.
523
524 **Lentiviral preparation and BMDM infection**
525 Second generation lentiviral particles were prepared by co-transfecting HEK-293T cells with plasmid
526 of interest, relative packaging and envelope. 48 hours after transfection, supernatant-containing
527 virus was collected, centrifuged 300g for 5' to remove cell debris and filtered through 0.45 µm filter.
528 Cleared supernatants were mixed with Lenti-X concentrator (Takara) and concentrated 100x,
529 following manufacturer instructions. 20 µL of concentrated lentiviral particles were used to infect 2
530 x 10^6 BMDM at day 4 in a 6-well plate. At day 6, viral-containing supernatant was removed and
531 attached cells were washed 2x in sterile PBS. Infected BMDM were used at day 7 after two more
532 washes in PBS to get rid of any remaining viral particle. Plasmid used for generation of lentivectors
533 were the following: pMD2.G (Addgene #12259), psPAX2 (Addgene #12260), SEWW-eGFP-WASp
534 (Blundell et al., 2008), pCDH-NLS-GFP (Addgene #132772), pTRIP-mCherry-FLAG-cGAS
535 E225A/D227A (Addgene #127657).
536
537 **CRISPR-Cas9 RNPs electroporation**
538 CRISPR-Cas9-mediated gene knock-out was achieved through electroporation of ribonucleoprotein
539 (RNP) particles containing crRNA, tracRNA and Cas9 protein complexes. spCas9 and RNA oligos were
540 purchased from IDT, annealed and mixed following manufacturer instructions. At day 4 of
541 differentiation, 1.5 x 10^6 cells were electroporated in 100 µL of media in a NEPA electroporator with
542 the following parameters: poring pulse 275 V, 4 x 1 ms, interval 50 ms, D. Rate 10 %; transfer pulse
543 20 V, 5 x 50 ms, interval 50 ms, D. Rate 40 %, polarity +/-. After 24 h media was changed and cells
544 were used for experiments at day 7 of differentiation.

545

546 **6-well plate confiner**

547 Mechanical confinement was performed in 6-well plates (Liu et al., 2015). 12 mm glass coverslips
548 were washed with hand soap, rinsed in ddH_2O, then in isopropanol and dried with a pressurized air
549 gun. The clean coverslips were treated in a plasma cleaner (Diener Zepto) at 40W for 30 s. To make
550 pillars of desired height, polydimethylsiloxane (PDMS; SYLGARD 184, Dow) was mixed at a ratio of
551 PDMS A:cross-linker B 1:10 (wt/wt) and poured on top of wafer molds-containing pillars of 3 µm or
552 6 µm. The wafer molds, containing pillars of 3 µm or 6 µm, were fabricated by conventional
553 micromachining from square pieces (25x25 mm) of a 500 µm thick silicon wafer. After cleaning the
554 wafer with acetone and isopropanol, a positive photoresist MEGAPOSIT™ SPR™220 3.0 or 7.0 was
555 spinned on. After the soft bake, they were exposed to a UV lamp for 30 seconds with a suitable mask
556 and subjected a post-bake process. The development was carried out with MF24A. To functionalized
557 with micropillars, glass coverslips were pressed to the wafers and baked at 85°C for 20 min before
558 being carefully detached with a blade. After a wash in isopropanol, coverslips with micropillars were
559 dried and plasma treated for 30 more seconds. Finally, these coverslips were washed in PBS and
560 incubated with non-adhesive PEG solution (Sigma) 500 µg/mL in PBS for 30 min at RT and UV-
561 sterilized for 20'. Before confinement, functionalized glass coverslips were washed in H_2O and PBS
562 and kept in sterile PBS at 4°C for a maximum of 48 h. To perform confinement experiments, we used
563 large PDMS pistons placed on the plate lid to press the coverslips on the bottom of the plate. A drop
564 of 250 µL containing 300.000 cells for immunofluorescent assays or 500.000 cells for RNA collection
565 was confined for each well. 6-well plates with a glass bottom were used for cell imaging (MatTek,
566 P06G-1.5-20-F); whereas non-treated 6-well plates (Corning) were adopted for RNA experiments.
567 Nuclear blebbing quantification was performed right after confinement on live cells based on
568 Hoechst 33342 staining (1:10.000 in PBS). Both types of confinements were kept for 1 h before
569 fixation or RNA extraction. Fixation for IF was performed directly on confined cells, by leaving 4%
570 PFA for 45 min before removing the lid, quenching PFA with 0,1 M glycine in PBS and washing cells
571 3x with PBS before proceeding with IF staining.

572

573 **Microchannel preparation and live imaging**

574 Microchannels MC004 were purchased from 4DCell. And prepared following manufactures
575 instructions. Coating was performed using 10 µg/mL fibronectin for 1 h at RT. Before utilization,
576 channels were incubated from 30 min to overnight in 2 mL of BMDM media. Timelapse imaging was

577 carried out overnight on a Nikon Eclipse TiE inverted microscope equipped with a 20x/0.75 NA dry
578 objective, a motorized stage and a humidified chamber at 37°C and 5% CO_2. Live imaging of migrating
579 macrophages in microchannels was recorded with a frame every 5 min, based on NLS-GFP (FITC
580 channel) and DIC (transmitted light). After overnight migration, cells inside channels were fixed by
581 adding 10 µL of 4% PFA to each accession port and waiting for 1 h at RT before washing in PBS.
582 Channels were kept in PBS 0,02% Sodium Azide until further imaging. Hoechst 1:1000 in PBS was
583 added for at least 1 h before imaging fixed microchannels to facilitate detection and segmentation
584 of nuclear morphology and herniations Fixed samples were imaged on a Zeiss LSM880 confocal
585 microscope with a 63x/1.4 NA oil objective for individual nuclei and a 20x/0.60 NA dry objective for
586 large field acquisitions and quantification of cell entry.
587
588 **Immunofluorescence imaging**
589 Immunofluorescence staining at steady state was done with 50.000 BMDM seeded on fibronectin-
590 coated (10ug/mL, Millipore Sigma) 12 mm microscope slides (Epredia, Thickness value #1). Cells
591 were left 30' at 37°C and 5% CO_2 to adhere. Fixation was performed in 4% PFA for 7 min at RT,
592 followed by quenching in 0,1 M glycine in PBS for 3 min. After 3x washes in PBS, cells were
593 permeabilized in PBS 1% BSA, 0,1% Triton-X100, blocked in PBS 3% BSA, 10 mM Hepes and stained
594 ON at 4°C in primary antibodies diluted in PBS 0,2% BSA, 0,1% Triton-X100. Secondary antibodies
595 were incubated at RT for 2h, followed by eventual phalloidin staining (Thermo Fischer Scientific, used
596 1:500) and 10 min nuclear staining with Hoechst 33342 (Invitrogen) 1:1000 in PBS. Slides were
597 mounted with Mowiol and imaged at Zeiss LSM880 confocal microscope with a 63x/1.4 NA oil
598 objective, or a 20x/0.60 NA dry objective. A full list of antibodies, dyes and probes used is presented
599 in supplementary table 6.
600
601 **AFM based indentation measurements**
602 AFM-based indentation measurements were performed by NanoWizard III AFM (JPK Instruments,
603 Bruker) integrated with an inverted optical microscope (Axiovert 200; Zeiss) for sample observation.
604 Cells were analysed in petri-dish and in culture medium at room temperature. The status of cells
605 was constantly monitored by optical microscope. Indentation of the whole cell body was performed
606 using MLCT-SPH-5um probes (Bruker), which have a cylindrical tip shank ending in a spherical tip
607 with a 5 µm radius and a nominal spring constant of 0.06 N/m. Once localized the cell by optical
608 microscope, the probe was brought over the nucleus area and pressed down to indent the cell. The

609 motion of the z-piezo and the force were recorded. On each cell three to five force–displacement (F-
610 D) curves were acquired with a force load of 0.5-1nN and at a rate of at 5µm/s in closed-loop
611 feedback mode. Cell elastic properties were assessed by determining the Young's modulus (E), which
612 can be evaluated by fitting the force (F) indentation (δ) curves with the Hertz model.
613
614 $$F = \frac{4}{3}\frac{E}{(1-\nu^2)}\sqrt{R}\delta^{3/2}$$
615
616 where F is the force, R is the radius of the spherical indenter and ν is the sample's Poisson ratio (set
617 to 0.5 for the cell) and δ is the indentation depth.
618 Data fitting was performed on the approaching F–D curves. JPK Data Processing software was used
619 to convert the F-D curves into the force–indentation curves by subtracting the cantilever bending
620 from the signal height to calculate indentation. The resulting force-indentation curves were fitted
621 with the Hertz model for indentation depth of 500 nm.
622
623 **Transwell migration assay**
624 24-well plates bearing transwell inserts of 5 µm and 3 µm. 5 µm plates were from Corning; 3 µm
625 plates from Thermo Fischer Scientific. At day 7 of differentiation, cells were detached using MACS
626 buffer (0,5% BSA, 2 mM EDTA in PBS), counted and resuspended in media without FBS containing
627 200 ng/mL of LPS (Invivogen) for 30 min in incubator. After LPS washout, cells were plated at a
628 concentration of 200.000 cells in 200 µL for each insert in complete media. On the bottom of each
629 well, 600 µL of complete media supplemented with 250 ng/mL of CCL19 (Peprotech) as
630 chemoattractant were added to promote transmigration. Cells were kept 5 h in incubator to allow
631 migration, following by collection of migrated cells for flow cytometry or IF analysis. Flow cytometry
632 quantification of migrating cells was performed at BD Accuri™ C6 flow cytometer, using Counting
633 Bright beads and normalizing the number of transmigrating cells to the total number of plated cells.
634
635 **Protein extraction and western blot**
636 Cells were lysed in an appropriated volume of RIPA buffer (50 mM Tris/HCl pH 7.5, 150 mM NaCl, 1%
637 NP-40, 0,1% SDS, 0,1% DOC in ddH_2O) supplemented 1:30 with protease inhibitor cocktail (Sigma
638 P8340). After centrifugation at 17000 g for 20 min, supernatant-containing protein extracts were
639 kept at -20°C until further processing. Total protein concentration was quantified by means of BCA
640 assay (Thermo Fisher), following manufacturer instructions. At least 20 µg of total protein lysates

641 were loaded on a 10% custom made polyacrylamide gel and transferred on PVDF membranes upon
642 SDS-page electrophoresis. Membranes were blocked at least 1 h at RT in 1x TBS, 0,1% Tween 20
643 (TBST), 3% dry fat milk. Primary antibodies were incubated ON at 4°C on a shaker. After 3x washes
644 in TBST, secondary HRP-conjugated antibodies were kept 1-2 h at RT. Chemiluminescence signal was
645 developed by Clarity ECL substrate (Bio-Rad) on a ChemiDoc™ Touch (Bio-Rad). A list of antibodies
646 used is reported in supplementary table 6.
647
648 **Library preparation and RNA-sequencing**
649 For mouse and human samples, total RNA was extracted using RNeasy Micro kit (Qiagen), according
650 to the manufacturer's protocol. RNA purity, integrity and quantity was checked at TapeStation 2200
651 (Agilent Technologies Inc., Santa Clara, CA, USA). RNA-seq libraries were prepared from 3 ng (human
652 PBMCs) or 5 ng (mouse BMDM) of total RNA using mRNA Library Prep Kit (WATCHMAKER) following
653 manufacture instruction. Briefly, we selected poly(A) using magnetic beads to focus sequencing on
654 polyadenylated transcripts. After RNA fragmentation, a step of cDNA synthesis was performed. The
655 resulting fragments were used for A-tailing and were ligated to the adapters and Index Anchors
656 (TWIST bioscience, Twist universal system). PCR amplification (21 cycles) was performed to generate
657 the final indexed cDNA libraries. Individual library quantification and quality assessment was
658 performed using TapeStation 2200. Libraries were sent to Macrogen to be sequences on Novaseq
659 (Human PBMCs) or NovaseqX (Mouse BMDM) instrument on Illumina platform as paired end run
660 150 bp reads. A total of 6 PBMCs samples were sequenced before as well after gene therapy. Four
661 biological replicates of BMDM confined per genotype and three replicates for unconfined control
662 were sequenced.
663
664 **RNA-sequencing analysis**
665 Raw FastQ files were downloaded from Macrogen. Quality control, trimming and alignment were
666 performed using standard pipelines for FastQC, Trimgalore and STAR.
667 Confiner data: Raw reads count matrix outputs were imported and analysed in R software (R version
668 4.3.1). Normalized reads were obtained by standard DEseq2 functions and used for heatmaps
669 visualization. DESeq2 package (Love et al., 2014) was further used for differential gene expression
670 analysis. GSEA was performed on gseGO function of ClusterProfiler package on Log2FC ordered
671 genes with p-value cutoff of 0.01 and Benjamini-Hochberg p-value correction. DEGs were considered
672 as genes bearing p-value< 0.05 and a Log2FC> 1.2 or Log2FC< -1.2. GO analysis was performed on

673 DEGs using enrichGO function, based on biological processes, with a p-value cutoff of 0.05 and
674 Benjamini-Hochberg statistical correction. Visualizations of functional enrichment results were
675 obtained by ClusterProfiler and ggplot2 packages.
676 PBMCs data: DESeq2 analysis was performed starting on unnormalized reads comparing WAS pre-
677 vs post-gene therapy samples. gseGO from ClusterProfiler have been used to perform GSEA on
678 Log2FC ordered genes, using Entrez ID as key type, "BP" as ontology and 0.05 as p-value cutoff,
679 without further statistical correction methods. Full list of GSEA is available as Supplementary Table
680 7.
681 Analysis of publicly available dataset from GSE107963: Data were downloaded as TPM normalized
682 count matrix from GSE107963 (www.ncbi.nlm.nih.gov/geo/download/?acc=GSE107963, data
683 deposited on 15.12.2022 and downloaded on 13.08.2024). Samples used for analysis refer to 3
684 clones of a WT iPSC cell line (WASp +) and 3 isogenic CRISPR-Cas9-mediated Was KO iPSCs clones
685 (WASp -) differentiated into macrophages. TPM matrix was filtered and further processed to keep
686 only genes with non-zero reads. Log2(TPM+1) was used for heatmap visualization.
687
688 **Image analysis**
689 All raw images were analysed in Fiji ImageJ (Schindelin et al., 2012), using custom-written macros.
690 Lamin A/C alteration: Lamin A/C alteration score has been calculated based on standard deviation
691 (σ) of Lamin A/C signal. Nuclear segmentation has been based on Hoechst 33342 channel of z-
692 projected nuclei, with a size threshold > 10 μm^2, to exclude potential micronuclei from the analysis.
693 Alteration score has been plotted as σ/10. Masks of Lamin A/C wrinkles for representative pictures
694 has been obtained by an adaptive threshold method.
695 Chromocenters and H3K9me2 quantification: to quantify the number of chromocenters and the area
696 of peripheral heterochromatin, nuclei were first segmented based on Hoechst 33342 signal.
697 Chromocenters were detected based on an adaptive threshold and a size cutoff. Area of peripheral
698 heterochromatin has been calculated as the sum of chromocenters' area in close proximity to
699 nuclear edges, as those within 1 µm from nuclear borders. The same cutoff has been used for
700 H3K9me2 peripheral heterochromatin, measuring fluorescent intensity instead of chromocenters
701 area.
702 Microchannels analysis and WASp-GFP distribution: quantification of cells inside microchannels an
703 nuclear rupture events have been conducted manually. Kymographs of NLS-GFP migrating cells were
704 generated using a semi-automated macro in ImageJ. WASp-GFP distribution has been obtained in a

705 semi-automated way as follow. Briefly individually cropped cells inside channels were subjected to
706 automatic nuclear detection. Nuclear centre of mass was then moved to the centre of the image and
707 all individual cells were cropped and horizontally aligned. The size of the cells was normalized at 600
708 pixels and expanded 50 times before saving at a resolution size of 1200x200 pixels (w x h). Size
709 normalized cells were then merged by Stack>Z project>Average Intensity to obtain an average
710 intensity map profile of WASp distribution.
711
712 **Statistics**
713 Primary data were collected in Microsoft Excel and statistical analyses were performed using
714 GraphPad Prism version 9. For comparison between two or more groups with normally distributed
715 data two-tailed Student's T-test, one-way ANOVA or two-way ANOVA were used as appropriate. The
716 non-parametric Kruskal-Walli's test with Dunn's multiple comparison was performed to compare
717 three or more unmatched groups. In case of normalized values to 1 or 0, statistics has been
718 calculated by a one-sample t-test. *P* values <= 0.05 were considered significant, if not stated
719 differently.
720
721
722 ## Supplementary information
723 Description of supplementary data
724 - Supplementary table 1: Gene list of inflammatory signatures used in Fig.1
725 - Supplementary table 2: RNA-seq data normalized reads BMDM
726 - Supplementary table 3: RNA-seq data normalized reads PBMCs
727 - Supplementary table 4: Gene lists for signatures used in Fig.6
728 - Supplementary table 5: WAS patients' information
729 - Supplementary table 6: List of antibodies used in the work
730 - Supplementary Table 7: GSEA on WAS PBMCs dataset
731
732
733 ## Data availability
734 Sequencing data have been deposited at GEO database: BMDM confiner data (accession:
735 GSE285024), publicly available as of the 24/12/2024 and PBMCs WAS data (accession: GSE285174),
736 publicly available as of the 25/12/2024. Source data are provided in supplementary files. Any

additional information required to reanalyse the data reported in this paper is available from the lead contact upon formal request.

Author contributions

R.A, **G.M.P** and **F.B** conceived the study and designed the experiments. **R.A** performed most of the experiments, data analysis, and prepared the figures. **R.A** and **F.B** wrote the manuscript. **G.B** helped in the execution of experiments and performed WASp-GFP confinement. **Z.A** provided training and support for the confiner assays and helped in performing confiner experiments in Fig.4 (A, B and C). **M.M** assisted in image analysis. **G.M.P** and **L.L.R** assisted in the experimental part and critical discussion of the data. **G.M.P** prepared library for sequencing. **M.C** prepared photolithographic molds used for confiner slides fabrication. **L.A** performed and analysed atomic force microscopy. **M.C.C**, **F.F**, **A.A** and **A.V** provided human PBMCs samples. **A.-M.L.-D** critically discussed the data and the manuscript. **F.B** supervised the whole study. All authors read and approved the final version of the manuscript.

Disclosure and competing interest's statement

The authors declare no competing interests.

Acknowledgements

This work was supported by Telethon grant GGP20102 to **F.B**. **G.B**, **G.M.P** and **L.L.R**- were supported by ICGEB Arturo Falaschi pre- and post-doctoral fellowships. **R.A** was supported by Italian Telethon. **R.A** received an EMBO scientific exchange grant (10017) to perform part of the work in the lab of **A.-M.L.-D**. We Thank Luca Triboli from ICGEB Trieste to help discussing bioinformatic data analysis.

769 ## References

770 Ablasser, A., and Gulen, M. F. (2016). The role of cGAS in innate immunity and beyond. *J. Mol. Med.* 94,
771 1085–1093. doi:10.1007/s00109-016-1423-2.

772 Alraies, Z., Rivera, C. A., Delgado, M. G., Sanséau, D., Maurin, M., Amadio, R., et al. (2024). Cell shape
773 sensing licenses dendritic cells for homeostatic migration to lymph nodes. *Nat. Immunol.* 25.
774 doi:10.1038/S41590-024-01856-3.

775 Amadio, R., Piperno, G. M., and Benvenuti, F. (2021). Self-DNA Sensing by cGAS-STING and TLR9 in
776 Autoimmunity : Is the Cytoskeleton in Control ? *Front. Immunol.* 12. doi:10.3389/fimmu.2021.657344.

777 Bastianello, G., Porcella, G., Beznoussenko, G. V., Kidiyoor, G., Ascione, F., Li, Q., et al. (2023). Cell stretching
778 activates an ATM mechano-transduction pathway that remodels cytoskeleton and chromatin. *Cell*
779 *Rep.* 42, 113555. doi:10.1016/j.celrep.2023.113555.

780 Bell, E. S., Shah, P., Zuela-Sopilniak, N., Kim, D., Varlet, A.-A. A., Morival, J. L. P. P., et al. (2022). Low lamin A
781 levels enhance confined cell migration and metastatic capacity in breast cancer. *Oncogene* 41, 1–20.
782 doi:10.1038/S41388-022-02420-9.

783 Blundell, M. P., Bouma, G., Calle, Y., Jones, G. E., Kinnon, C., and Thrasher, A. J. (2008). Improvement of
784 Migratory Defects in a Murine Model of Wiskott–Aldrich Syndrome Gene Therapy. *Mol. Ther.* 16, 836–
785 844. doi:10.1038/MT.2008.43.

786 Blundell, M. P., Worth, A., Bouma, G., and Thrasher, A. J. (2010). The Wiskott-Aldrich syndrome: The actin
787 cytoskeleton and immune cell function. *Dis. Markers* 29, 157–175. doi:10.3233/DMA-2010-0735.

788 Calixto Vieira, R., Goncalves, L., Westerberg, L. S., Rhaissa, C., Vieira, C., and Goncalves Pinho, L. (2023).
789 Understanding immunoactinopathies: A decade of research on WAS gene defects. *Pediatr. Allergy*
790 *Immunol.* 34, e13951. doi:10.1111/PAI.13951.

791 Cervantes-Luevano, K. E., Caronni, N., Castiello, M. C., Fontana, E., Piperno, G. M., Naseem, A., et al. (2018).
792 Neutrophils drive type I interferon production and autoantibodies in patients with Wiskott-Aldrich
793 syndrome. *J. Allergy Clin. Immunol.* 142, 1605-1617.e4. doi:10.1016/j.jaci.2017.11.063.

794 Davidson, P. M., Denais, C., Bakshi, M. C., and Lammerding, J. (2014). Nuclear deformability constitutes a
795 rate-limiting step during cell migration in 3-D environments. *Cell. Mol. Bioeng.* 7, 293.
796 doi:10.1007/S12195-014-0342-Y.

797 De Silva, N. S., Siewiera, J., Alkhoury, C., Nader, G. P. F., Nadalin, F., de Azevedo, K., et al. (2023). Nuclear
798 envelope disruption triggers hallmarks of aging in lung alveolar macrophages. *Nat. Aging* 3, 1251–
799 1268. doi:10.1038/s43587-023-00488-w.

800 Decout, A., Katz, J. D., Venkatraman, S., and Ablasser, A. (2021). The cGAS–STING pathway as a therapeutic
801 target in inflammatory diseases. *Nat. Rev. Immunol.* doi:10.1038/s41577-021-00524-z.

802 Delgado, M.-G. et al. (2024). The Arp2/3 complex maintains the epidermal Langerhans cell network and
803 DNA integrity. *Under Submiss.*

804 Denais, C. M., Gilbert, R. M., Isermann, P., McGregor, A. L., Te Lindert, M., Weigelin, B., et al. (2016).
805 Nuclear envelope rupture and repair during cancer cell migration. *Science (80-.).* 352. Available at:
806 /pmc/articles/PMC4833568/ [Accessed March 24, 2023].
807 Dou, Z., Ghosh, K., Vizioli, M. G., Zhu, J., Sen, P., Wangensteen, K. J., et al. (2017). Cytoplasmic chromatin
808 triggers inflammation in senescence and cancer. *Nature* 550. doi:10.1038/nature24050.
809 Dunphy, G., Flannery, S. M., Almine, J. F., Connolly, D. J., Paulus, C., Jønsson, K. L., et al. (2018). Non-
810 canonical Activation of the DNA Sensing Adaptor STING by ATM and IFI16 Mediates NF-κB Signaling
811 after Nuclear DNA Damage. *Mol. Cell*. doi:10.1016/j.molcel.2018.07.034.
812 En, A., Bogireddi, H., Thomas, B., Stutzman, A. V., Ikegami, S., LaForest, B., et al. (2024). Pervasive nuclear
813 envelope ruptures precede ECM signaling and disease onset without activating cGAS-STING in Lamin-
814 cardiomyopathy mice. *Cell Rep.* 43, 114284. doi:10.1016/j.celrep.2024.114284.
815 Gaertner, F., Reis-Rodrigues, P., de Vries, I., Hons, M., Aguilera, J., Riedl, M., et al. (2022). WASp triggers
816 mechanosensitive actin patches to facilitate immune cell migration in dense tissues. *Dev. Cell* 57, 47-
817 62.e9. doi:10.1016/j.devcel.2021.11.024.
818 Ginhoux, F., and Guilliams, M. (2016). Tissue-Resident Macrophage Ontogeny and Homeostasis. *Immunity*
819 44, 439–449. doi:10.1016/j.immuni.2016.02.024.
820 Harada, T., Swift, J., Irianto, J., Shin, J. W., Spinler, K. R., Athirasala, A., et al. (2014). Nuclear lamin stiffness
821 is a barrier to 3D migration, but softness can limit survival. *J. Cell Biol.* 204, 669.
822 doi:10.1083/JCB.201308029.
823 Härtlova, A., Erttmann, S. F., Raffi, F. A. M., Schmalz, A. M., Resch, U., Anugula, S., et al. (2015). DNA
824 Damage Primes the Type I Interferon System via the Cytosolic DNA Sensor STING to Promote Anti-
825 Microbial Innate Immunity. *Immunity* 42, 332–343. doi:10.1016/j.immuni.2015.01.012.
826 Kim, J. K., Louhghalam, A., Lee, G., Schafer, B. W., Wirtz, D., and Kim, D. H. (2017). Nuclear lamin A/C
827 harnesses the perinuclear apical actin cables to protect nuclear morphology. *Nat. Commun. 2017 81* 8,
828 1–13. doi:10.1038/s41467-017-02217-5.
829 Kovacs, M. T., Vallette, M., Wiertsema, P., Dingli, F., Loew, D., Nader, G. P. de F., et al. (2023). DNA damage
830 induces nuclear envelope rupture through ATR-mediated phosphorylation of lamin A/C. *Mol. Cell* 83,
831 3659. doi:10.1016/J.MOLCEL.2023.09.023.
832 Le, H. Q., Ghatak, S., Yeung, C. Y. C., Tellkamp, F., Günschmann, C., Dieterich, C., et al. (2016). Mechanical
833 regulation of transcription controls Polycomb-mediated gene silencing during lineage commitment.
834 *Nat. Cell Biol.* 18, 864–875. doi:10.1038/ncb3387.
835 Lee, P. P., Lobato-Márquez, D., Pramanik, N., Sirianni, A., Daza-Cajigal, V., Rivers, E., et al. (2017). Wiskott-
836 Aldrich syndrome protein regulates autophagy and inflammasome activity in innate immune cells.
837 *Nat. Commun.* 8, 1–13. doi:10.1038/s41467-017-01676-0.
838 Liang, F., Peng, C., Luo, X., Wang, L., Huang, Y., Yin, L., et al. (2023). A single-cell atlas of immunocytes in the

839 spleen of a mouse model of Wiskott-Aldrich syndrome. *Cell. Immunol.*, 104783.
840 doi:10.1016/j.cellimm.2023.104783.
841 Linder, S., Nelson, D., Weiss, M., and Aepfelbacher, M. (1999). Wiskott-Aldrich syndrome protein regulates
842 podosomes in primary human macrophages. *Cell Biol. Commun. by John A. Glomset* 96, 9648–9653.
843 Available at: www.pnas.org. [Accessed March 9, 2022].
844 Liu, Y. J., Le Berre, M., Lautenschlaeger, F., Maiuri, P., Callan-Jones, A., Heuzé, M., et al. (2015).
845 Confinement and low adhesion induce fast amoeboid migration of slow mesenchymal cells. *Cell* 160,
846 659–672. doi:10.1016/j.cell.2015.01.007.
847 Love, M. I., Huber, W., and Anders, S. (2014). Moderated estimation of fold change and dispersion for RNA-
848 seq data with DESeq2. *Genome Biol.* 15, 1–21. doi:10.1186/s13059-014-0550-8.
849 Maekawa, H., Inoue, T., Ouchi, H., Jao, T. M., Inoue, R., Nishi, H., et al. (2019). Mitochondrial Damage
850 Causes Inflammation via cGAS-STING Signaling in Acute Kidney Injury. *Cell Rep.* 29, 1261-1273.e6.
851 doi:10.1016/j.celrep.2019.09.050.
852 Magnani, A., Semeraro, M., Adam, F., Booth, C., Dupré, L., Morris, E. C., et al. (2022). Long-term safety and
853 efficacy of lentiviral hematopoietic stem/progenitor cell gene therapy for Wiskott-Aldrich syndrome.
854 *Nat. Med.* 28. doi:10.1038/s41591-021-01641-x.
855 Mu, X., Tseng, C., Hambright, W. S., Matre, P., Lin, C. Y., Chanda, P., et al. (2020). Cytoskeleton stiffness
856 regulates cellular senescence and innate immune response in Hutchinson–Gilford Progeria Syndrome.
857 *Aging Cell* 19, 1–16. doi:10.1111/acel.13152.
858 Mukherjee, S., Abdisalaam, S., Bhattacharya, S., Srinivasan, K., Sinha, D., and Asaithamby, A. (2019).
859 "Mechanistic link between DNA damage sensing, repairing and signaling factors and immune
860 signaling," in *Advances in Protein Chemistry and Structural Biology* (Academic Press Inc.), 297–324.
861 doi:10.1016/bs.apcsb.2018.11.004.
862 Naseem, A., Steinberg, Z., and Cavazza, A. (2022). Genome editing for primary immunodeficiencies: A
863 therapeutic perspective on Wiskott-Aldrich syndrome. *Front. Immunol.* 0, 4553.
864 doi:10.3389/FIMMU.2022.966084.
865 Nava, M. M., Miroshnikova, Y. A., Biggs, L. C., Whitefield, D. B., Metge, F., Boucas, J., et al. (2020).
866 Heterochromatin-Driven Nuclear Softening Protects the Genome against Mechanical Stress-Induced
867 Damage. *Cell* 181, 800. doi:10.1016/J.CELL.2020.03.052.
868 Oliveira, M. M. S., Kung, S. Y., Moreau, H. D., Maurin, M., Record, J., Sanséau, D., et al. (2022). The WASp
869 L272P gain-of-function mutation alters dendritic cell coordination of actin dynamics for migration and
870 adhesion. *J. Leukoc. Biol.* 111, 793–803. doi:10.1002/JLB.1AB0821-013RR.
871 Patteson, A. E., Vahabikashi, A., Pogoda, K., Adam, S. A., Mandal, K., Kittisopikul, M., et al. (2019). Vimentin
872 protects cells against nuclear rupture and DNA damage during migration. *J. Cell Biol.* 218, 4079–4092.
873 doi:10.1083/JCB.201902046.

874 Piperno, G. M., Naseem, A., Silvestrelli, G., Amadio, R., Caronni, N., Cervantes-Luevano, K. E., et al. (2020).
875 Wiskott-Aldrich syndrome protein restricts cGAS/STING activation by dsDNA immune complexes. *JCI*
876 *Insight* 5. doi:10.1172/jci.insight.132857.
877 Prete, F., Catucci, M., Labrada, M., Gobessi, S., Castiello, M. C., Bonomi, E., et al. (2013). Wiskott-Aldrich
878 syndrome protein-mediated actin dynamics control type-I interferon production in plasmacytoid
879 dendritic cells. *J. Exp. Med.* 210, 355–374. doi:10.1084/jem.20120363.
880 Reis-rodrigues, P., Canigova, N., Avellaneda, M. J., Gaertner, F., Vaahtomeri, K., Riedl, M., et al. (2024).
881 Global coordination of protrusive forces in migrating immune cells. *bioRxiv*.
882 Rodríguez-Nuevo, A., Díaz-Ramos, A., Noguera, E., Díaz-Sáez, F., Duran, X., Muñoz, J. P., et al. (2018).
883 Mitochondrial DNA and TLR9 drive muscle inflammation upon Opa1 deficiency. *EMBO J.* 37.
884 doi:10.15252/embj.201796553.
885 Schindelin, J., Arganda-Carreras, I., Frise, E., Kaynig, V., Longair, M., Pietzsch, T., et al. (2012). Fiji: An open-
886 source platform for biological-image analysis. *Nat. Methods* 9, 676–682. doi:10.1038/nmeth.2019.
887 Sereni, L., Castiello, M. C., Di Silvestre, D., Della Valle, P., Brombin, C., Ferrua, F., et al. (2019). Lentiviral
888 gene therapy corrects platelet phenotype and function in patients with Wiskott-Aldrich syndrome. *J.*
889 *Allergy Clin. Immunol.* 144, 825–838. doi:10.1016/j.jaci.2019.03.012.
890 Sereni, L., Castiello, M. C., Marangoni, F., Anselmo, A., di Silvestre, D., Motta, S., et al. (2018). Autonomous
891 role of Wiskott-Aldrich syndrome platelet deficiency in inducing autoimmunity and inflammation. *J.*
892 *Allergy Clin. Immunol.* 142, 1272–1284. doi:10.1016/j.jaci.2017.12.1000.
893 Shen, C., Postat, J., Cerf, A., Merino, M., Bhagrath, A., Patel, D., et al. (2024). DOCK8 regulates a
894 mechanosensitive actin redistribution that maintains immune cell cohesion and protects the nucleus
895 during migration. *bioRxiv*, 2024.07.26.605273. Available at:
896 https://www.biorxiv.org/content/10.1101/2024.07.26.605273v1%0Ahttps://www.biorxiv.org/content
897 /10.1101/2024.07.26.605273v1.abstract.
898 Sladitschek-Martens, H. L., Guarnieri, A., Brumana, G., Zanconato, F., Battilana, G., Xiccato, R. L., et al.
899 (2022). YAP/TAZ activity in stromal cells prevents ageing by controlling cGAS–STING. *Nature* 607, 790–
900 798. doi:10.1038/s41586-022-04924-6.
901 Snapper, S. B., Rosen, F. S., Mizoguchi, E., Cohen, P., Khan, W., Liu, C. H., et al. (1998). Wiskoff-Aldrich
902 syndrome protein-deficient mice reveal a role for WASP in T but not B cell activation. *Immunity* 9, 81–
903 91. doi:10.1016/S1074-7613(00)80590-7.
904 Song, X., Aw, J. T. M., Ma, F., Cheung, M. F., Leung, D., and Herrup, K. (2021). DNA repair inhibition leads to
905 active export of repetitive sequences to the cytoplasm triggering an inflammatory response. *J.*
906 *Neurosci.* 41, 9286–9307. doi:10.1523/JNEUROSCI.0845-21.2021.
907 Sudhakar, M., Rikhi, R., Loganathan, S. K., Suri, D., and Singh, S. (2021). Autoimmunity in wiskott–aldrich
908 syndrome: Updated perspectives. *Appl. Clin. Genet.* 14, 363–388. doi:10.2147/TACG.S213920.

Tang, W., Chen, X., Wang, X., Zhu, M., Shan, G., Wang, T., et al. (2023). Indentation induces instantaneous nuclear stiffening and unfolding of nuclear envelope wrinkles. *Proc. Natl. Acad. Sci. U. S. A.* 120, e2307356120. Available at: https://www.pnas.org/doi/abs/10.1073/pnas.2307356120 [Accessed November 7, 2023].

Thiam, H. R., Vargas, P., Carpi, N., Crespo, C. L., Raab, M., Terriac, E., et al. (2016). Perinuclear Arp2/3-driven actin polymerization enables nuclear deformation to facilitate cell migration through complex environments. *Nat. Commun.* 7, 1–14. doi:10.1038/ncomms10997.

Vargas, P., Chabaud, M., Thiam, H. R., Lankar, D., Piel, M., and Lennon-Dumenil, A. M. (2016). Study of dendritic cell migration using micro-fabrication. *J. Immunol. Methods* 432, 30–34. doi:10.1016/J.JIM.2015.12.005.

Xian, H., Watari, K., Sanchez-Lopez, E., Offenberger, J., Onyuru, J., Sampath, H., et al. (2022). Oxidized DNA fragments exit mitochondria via mPTP- and VDAC-dependent channels to activate NLRP3 inflammasome and interferon signaling. *Immunity* 55, 1370-1385.e8. doi:10.1016/j.immuni.2022.06.007.

Yuan, B., Zhou, X., Suzuki, K., Ramos-Mandujano, G., Wang, M., Tehseen, M., et al. (2022). Wiskott-Aldrich syndrome protein forms nuclear condensates and regulates alternative splicing. *Nat. Commun. 2022 131* 13, 1–20. doi:10.1038/s41467-022-31220-8.

944 ## Figures and Figure legends

945

946 **Figure 1 – WASp deficiency correlates to enhanced expression of inflammatory genes in**
947 **macrophages**. (**A**) Alveolar macrophages (AMO) from 10 weeks old mice were harvested and
948 processed for flow cytometry. Data show mean fluorescent intensity (MFI) of CD86. Data are from
949 one representative of two experiments (n=3 mice per genotype). Two-tailed unpaired t-test;
950 ***P*<=0.01. (**B**) Quantification of AMO total numbers in 10- and 25-weeks-old adult mice (n=3 mice,
951 data are from one representative of two experiments). One-way ANOVA test with multiple
952 comparisons, **P*<=0.05. (**C**) Inflammatory genes expression in AMO. mRNA expression (RT-qPCR,
953 plotted as fold to WT) of the indicated genes in sorted AMO from 10-and 25-weeks-old WKO mice.
954 n=3 mice for each condition, one sample t-test, **P*<=0.05. (**D**) Inflammatory genes in primary bone
955 marrow-derived macrophages (BMDM). RT-qPCR values in WKO are plotted as fold to WT. Number
956 of biological replicates are: Tnfa and Il1b (n=3); Ifnb1 (n=4); Mx1 (n=5); Il6 and Isg15 (n=8). One
957 sample t-test. **P*<=0.05, ***P*<=0.01. (**E**) Expression of an inflammatory signature (list of genes used
958 to calculate inflammatory z-score can be found in Supplementary Table 1) on the GSE107963
959 dataset. Control (WASp +) or gene-edited (WASp -) human iPSCs-derived macrophages. (**F**) Heatmap
960 of selected inflammatory genes expression (Log2+1 TPM normalized expression, z-score gene-wise
961 scaled) of WT and WASp KO iPSCs-derived macrophages from GSE107963. (**G**) Inflammatory score
962 in PBMC of a cohort of 6 WAS patients before (WASp -) and after restoration of WASp by gene
963 therapy (WASp +). (**H**) Heatmap of selected inflammatory genes expression (Log2+1 normalized
964 reads, z-score gene-wise scaled) in human PBMCs from WAS patients pre- and post- gene therapy.

965

966

967 **Supplementary Figure 1 - WASp reduces steady state inflammatory activation of macrophages in-**
968 **vivo and in-vitro**. (**A**) Flow cytometry gating strategy to identify AMO in mouse lung tissues. (**B**) GSEA
969 analysis of relevant modulated pathways in WAS PBMCs before and after gene therapy correction.
970 Values are expressed as normalized enrichment score. (**C**) Expression of the indicated genes in
971 individual PBMC samples pre- and post-gene therapy. Data are plotted as Log2 FC post vs pre gene
972 therapy, each dot is a patient. One sample t-test; **P*<=0.05 and ***P*<=0.01. (**D**) RT-qPCR validation
973 of selected inflammatory genes in 6 WAS patients pre- and post-gene therapy. The dotted line
974 represents the mean gene expression of 3 healthy donor controls (HC). One sample t-test: **P*<=0.05.
975 (**E**) Correlation between inflammatory score (IS) before WASp restoration (y-axis) and IS reduction

976 (Δ IS) upon WASp re-expression (x-axis). Data combines 3 human iPSCs-derived macrophages and 6
977 human PBMCs. Data were analysed by linear regression; *P*=0.0095.
978
979
980 **Figure 2 –Nuclear parameters are modified in WASp null macrophages**. (**A**) WT and WKO BMDM
981 were plated on glass and labelled with Hoechst to visualise nuclei. Representative images show
982 examples of the three parameters analysed: area (top), roundness (middle) and micronuclei
983 (bottom). Scale bar 10 µm. (**B**) Quantification of the three nuclear parameters depicted in A, each
984 dot is an independent experiment (*N*=6 experiments with *n*>2000 nuclei analysed for each
985 genotype). Two-tailed unpaired t-test; **P*<=0.05. (**C**) Representatives immunoblot (top left) and
986 relative quantification of LMNA/C protein expression relative to GAPDH (top right); *n*=3 biological
987 replicates. Data were analysed by one sample t-test. **P*<0.05. (**D**) Expression of lamin isoforms from
988 RNA-seq analysis of WT and WKO BMDM. Normalized reads for Lamin A/C, LMNB isoforms 1 and 2
989 and Emerin. Representative data from *n*=2 replicates. Data were analysed by two-way ANOVA test
990 with multiple comparisons and Sidak's correction method. *****P*<=0.0001. (**E**) Representatives
991 maximum z-projection of Lamin A/C staining (top) and the corresponding segmentation mask for
992 wrinkles detection (bottom). Quantification of LMNA/C alterations as defined in methods. A higher
993 score indicates less homogeneity and more wrinkles. *n*=405 WT and *n*=308 WKO individual nuclei
994 measured, in 3 independent experiments. Scale bar 5 µm. Two-tailed unpaired t-test, **** =
995 *P*<0.0001. (**F**) Representative images of Lamin A/C (grey) and Emerin (red) co-staining (top) and line
996 intensity profiles (bottom). Histograms depict areas of colocalization at nuclear boundaries (blue
997 area) and in nuclear wrinkles (red area). Three independent co-labelling experiments were
998 performed. Scale bar 5 µm.
999
1000
1001 **Supplementary Figure 2 – Chromatin features and cellular mechanics in WT and WASp KO**
1002 **macrophages**. (**A**) Representative images (left) and quantification (right) of the number of
1003 chromocenters (heterochromatin foci) in WT and WKO BMDM nuclei and the mean area of
1004 peripheral heterochromatin foci. *n*=65 individual nuclei measured from *N*=3 independent
1005 experiments. Scale bar 5 µm. Statistics was calculated by two-tailed unpaired t-test. ns, not
1006 significant. (**B**) Representative images (left) and quantification (right) of mean fluorescent intensity
1007 and ratio of peripheral vs central H3K9me2 marker of facultative heterochromatin. *N*=3 independent

1008 experiments, with *n*=65 individual nuclei measured in total. Data were analysed by two-tailed
1009 unpaired t-test. ****P*<=0.001; ns, not significant. Scale bar 5 µm. (**C**) Scheme of AFM-indentation
1010 measurement of a single BMDM cell. Bright field image scale bar 50 µm (**D**) Quantification of Young's
1011 modulus of *n*=71 WT and *n*=62 WKO BMDM cells, from three independent measurements. Data
1012 were analysed by two-tailed unpaired t-test. ****P*<=0.001.
1013
1014
1015 **Figure 3 – WASp controls the deformation and integrity of the nucleus during migration in**
1016 **microchannels**. (**A**) Analysis of nuclear parameters in macrophages migrating through 2-8 µm x 5
1017 µm fibronectin coated micro-channels. Representative images of nuclei within channels after
1018 overnight migration (applying a nuclear mask). (**B**) Entrance rate of the two genotypes inside
1019 channels of different dimensions. Data are from *N*=3 and *N*=4 independent experiments for WT and
1020 WKO, respectively. Data were analysed by two-way ANOVA test, **P*<=0.05. (**C**) Representative
1021 examples of WT and WKO macrophage nuclei inside 6 µmx5µm channels (left). Corresponding
1022 quantification of the fraction of cells showing herniated nuclei (right). *n*=40 WT and 57 WKO cells in
1023 *N*=3 independent experiment, two-tailed unpaired t-test. (**D**) Quantification of the position of the
1024 herniation relative to the direction of migration, two-way ANOVA with Sidak's correction method.
1025 ns, not significant. (**E**) WT and WKO BMDM were transduced with NLS-GFP to track nuclear rupture
1026 during migration. (**F**) Representative time frames (top) and relative kymographs (bottom) showing a
1027 nuclear rupture event in WKO migrating inside 6 µm x 5 µm channels, detected as cytosolic leakage
1028 of NLS-GFP. Scale bar 10 µm. (**G**) Quantification of the fraction of cells undergoing nuclear rupture
1029 during live imaging. *N*=3 independent experiments, with at least 20 individual cells analysed per
1030 genotype for each experiment. Two-tails unpaired t-test. **P*<=0.05. (**H**) Quantification of multiple
1031 nuclear ruptures detected during live imaging experiments expressed as fraction of total ruptures
1032 recorded.
1033
1034
1035 **Supplementary Figure 3 – Constricted migration augments DNA damage in WKO cells**. (**A**)
1036 Schematic overview of nuclear mask segmentation from raw channel images and quantification of
1037 entrance rate as percent of cells inside channels and approaching cells. Approaching cells were
1038 defined as those present within 50 µm from channel beginning (yellow dashed line). (**B**) Schematic
1039 overview of transwell assay used for BMDCs migration (top) and relative quantification of

1040 transmigrating cells (bottom), in transwell of indicated pore size. *N*=3 independent replicates are
1041 plotted as normalized fold to respective WT (value=1). Statistics was calculated using a one-sample
1042 t-test. (**C**) Representative pictures of yH2AX staining pre and post 3 µm transwell migration in BMDCs
1043 and relative quantification of number of yH2AX foci per cell in WT and WKO. Data are from *N*=3
1044 independent experiments with *n*=178, 202 (WT and WKO pre transwell) and *n*=13, 33 (WT and WKO
1045 post transwell). **P*<=0.05 in a standard one-way ANOVA test. (**D**) Flow cytometry quantification of
1046 CCR7 median expression in WT and WKO BMDCs before 3 µm transwell migration and following 200
1047 ng/mL of LPS stimulation for 30' (*N*=3) or in unstimulated control (*N*=2). Statistics was performed
1048 comparing WT and WKO after LPS stimulation by an unpaired t-test. ns, not significant.
1049
1050
1051 **Figure 4 – Vertical confiners induce higher deformation and rupture in WASp-deficient**
1052 **macrophages.**
1053 (**A**) Representative images of WT and WKO macrophage's nuclei under 3 or 6 µm confinement
1054 height. Insets show nuclear deformation. On the right, representative examples of intact or damaged
1055 nuclei used for quantification. Scale bar 10 µm. (**B**) Quantification of the fraction of cells carrying a
1056 damaged nucleus after 1 h confinement at the indicated height. At least 200 cells per conditions
1057 were analysed in *N*=3 independent experiments. Two-tailed unpaired t-test. ****P*<=0.001. (**C**) Assay
1058 on NLS-GFP cytosolic release under confinement. Representative images of NLS-GFP$^+$ macrophages
1059 after 1h of confinement at 3 µm. Scale bar 20 µm. (**D**) Corresponding quantification of nuclear
1060 ruptures upon confinement based on NLS-GFP cytosolic leakage. Each dot is an independent
1061 experiment (*N*=3). *n*=173 WT and *n*=102 WKO cells. Data are expressed as fold to WT mean.
1062 **P*<=0.05 in a two-tailed unpaired t-test. (**E**) Individual frames from supplementary movie xx showing
1063 nuclear envelope rupture during live imaging. The timeframe is indicated by f; yellow arrow
1064 highlights bleb formation and subsequent rupture in WKO. (**F**) WKO cells transduced with WASP-GFP
1065 were subjected to confinement. Representative images of WASp-GFP$^+$ and WASp-GFP$^-$ macrophages
1066 after 1 h confinement at 3 µm. Dashed lines mark nuclear boundaries. Scale bar 20 µm; 5 µm for
1067 insets. (**G**) Corresponding quantification of nuclear blebbing in control or WASp-GFP reconstituted
1068 cells. Data are expressed as fold on WKO ctrl, *n*=83 WT and *n*=99 WKO cells from *N*=3 independent
1069 experiments, one sample t-test. ***P*<=0.01. (**H**). Representative images of confined (3µm) WASp-
1070 GFP$^+$ and WASp-GFP$^-$ macrophages stained for LMNA/C (yellow). Nuclear insets show LMNA/C and
1071 Hoechst signal in WKO ctrl (1) and WKO WASp-GFP (2). Scale bar 20 µm. (**I**) Quantification of LMNA/C

1072 rupture events in WKO ctrl and WKO WASp-GFP based on **H**. Data are from n=135 WKO ctrl and n=22
1073 WKO WASp-GFP in *N*=2 experiments.
1074
1075
1076 **Supplementary Figure 4 – WASp limits nuclear rupture under confinement**. (**A**) Cells were
1077 subjected to vertical confinement, as schematically represented. (**B**) Nuclear height quantification in
1078 2D without confinement in BMDM. Data from *N*=1 experiment with a total of 10 z-stacks nuclei
1079 measured for genotype. (**C**) Representative images of BMDM nuclear height from live-imaging
1080 acquisition of cell under confinement at 6 µm and 3 µm. Vertical scale bar 6 µm, with a tick every 1
1081 µm. (**D**) WKO BMDM were transduced with lentiviral particles encoding WASp-GFP. (**E**) Flow
1082 cytometry shows the fraction of WKO cells expressing WASp-GFP to visualize WASp-GFP expression.
1083 (**F**) Representatives immunoblot of WASp expression in WT, WKO ctrl and WKO WASp-GFP
1084 macrophages after 7 days of differentiation.
1085
1086
1087 **Figure 5 – WASp triggers perinuclear actin polymerization under confinement**. (**A**) Representative
1088 images of actin distribution in WT and WKO BMDM confined at 3 µm height. Scale bars 20 µm. (**B**)
1089 Quantification of the fraction of cells with central actin accumulation. n=number of cells, as indicated
1090 in figure. *N*=2 experiments for unconfined controls and *N*=4 for confined samples. Two-tailed
1091 unpaired t-test. ***P*<=0.01. (**C**) Representative images to define patterns of actin distribution in
1092 macrophages confined at 3µm. Scale bar 5 µm. (**D**) Corresponding quantification of the fraction of
1093 WT and WKO macrophages in each category. n=number of cells, as indicated in figure; from *N*=3
1094 individual experiments. (**E**) WKO cells transduced with WASp-GFP were confined at 3 µm and
1095 analysed to visualize the relative distribution of WASp and F-actin. Scale bar 5 µm. Line intensity
1096 profile of selected region showing the intensity distribution of WASp-GFP and phalloidin (bottom).
1097 (**F**) Quantification of WASp-GFP and F-actin Mander's coefficient of colocalization on perinuclear
1098 actin patches. Data are from **E**, with a total of *n*=20 cells analysed from *N*=2 independent
1099 experiments.
1100
1101
1102 **Supplementary Figure 5 – WASp perinuclear localization under confinement**.

1103 (**A**) WASp-GFP expressing cells were recorded during migration in 5 x 6 µm microchannels. (**B**) After
1104 fixation at the end of the recording period, WASp distribution was calculated by dividing the cell
1105 volume into three equal parts (top left). Average intensity map of WASp-GFP was obtained by
1106 normalizing and merging different cells from a fixed end time point analysis (bottom left). Data are
1107 from *n*=42 cells obtained in *N*=2 independent experiments. Representative line intensity profile of
1108 WASp-GFP signal (right).
1109
1110
1111 **Figure 6 – Mechanical confinement triggers innate activation in WASp KO macrophages**. (**A**) BMDM
1112 were subjected to 1 h confinement at 3 µm or kept in unconfined conditions and processed for RNA-
1113 seq and gene qPCR expression analysis. (**B**) Venn diagram of common and unique upregulated DEGs
1114 in WT and WKO BMDM confined at 3 µm as compared to their respective unconfined controls.
1115 Relevant processes and genes are highlighted. (**C**) Log2FC of commonly upregulated inflammatory
1116 genes by confinement in the two genotypes. (**D**) Z-score of branched actin signature across the two
1117 genotypes in unconfined and confined conditions (left). Normalized expression of relevant individual
1118 genes is showed as heatmap (right). (**E**) Z-score of nuclear mechanic signature across the two
1119 genotypes in unconfined and confined conditions (left). Normalized expression of relevant individual
1120 genes is showed as heatmap (right). (**F**) Z-score of NER induced inflammatory signature across the
1121 two genotypes in unconfined and confined conditions. *P* in **D**, **E**, and **F** were calculated by one-way
1122 ANOVA test. **P*<=0.05, ***P*<=0.01, ***P*<=0.001. (**G**) Quantification of Il-6 mRNA in confined WT and
1123 WKO BMDM after 1 h at indicated heights. *n*=6 for unconfined and 3 µm confined samples, *n*=4 for
1124 6 µm confined samples. ***P*<=0.01 on a one-way ANOVA test. (**H**) Normalized expression of Il-6
1125 mRNA in WT ctrl and WT WASp KO BMDM. Data from 6 individual confinement replicates. (**I**)
1126 Normalized expression of Il-6 mRNA in WKO ctrl and WKO STING KO BMDM from 4 individual
1127 confinement experiments. **P*<=0.05 on a one-sample t-test. (**J**) Model of WT and WKO macrophage
1128 response to confinement.
1129
1130
1131 **Supplementary Figure 6 – Mechanical confinement triggers innate activation in WASp KO**
1132 **macrophages**. (**A**) Venn diagram of differentially expressed genes between WT and WKO in
1133 unconfined resting condition. Relevant genes and processes are highlighted. (**B**) PCA analysis of
1134 BMDM unconfined controls and 3 µm confined samples from RNA-seq. (**C**) Venn diagram of DEGs

1135 downregulated by confinement in WT and WKO at 3 µm. Relevant genes are highlighted. (**D**) Z-score
1136 of Rac2 signature across the two genotypes in unconfined and confined conditions (left). Normalized
1137 expression of Sun2/RhoA/ROCK genes is showed as heatmap (right). (**E**) Representative western blot
1138 of KO efficiency control in WT macrophages after 72 h from sgCtrl or sgWASp CRISPR-Cas9
1139 electroporation. (**F**) Representative western blot for KO efficiency in WKO macrophages after sgCtrl
1140 or sgSTING CRISPR-Cas9. (**G**) Il6 quantification in WKO and WKO STING KO at steady state and upon
1141 direct STING stimulation by 3 µg/mL of DMXAA.
1142
1143

Figure 1

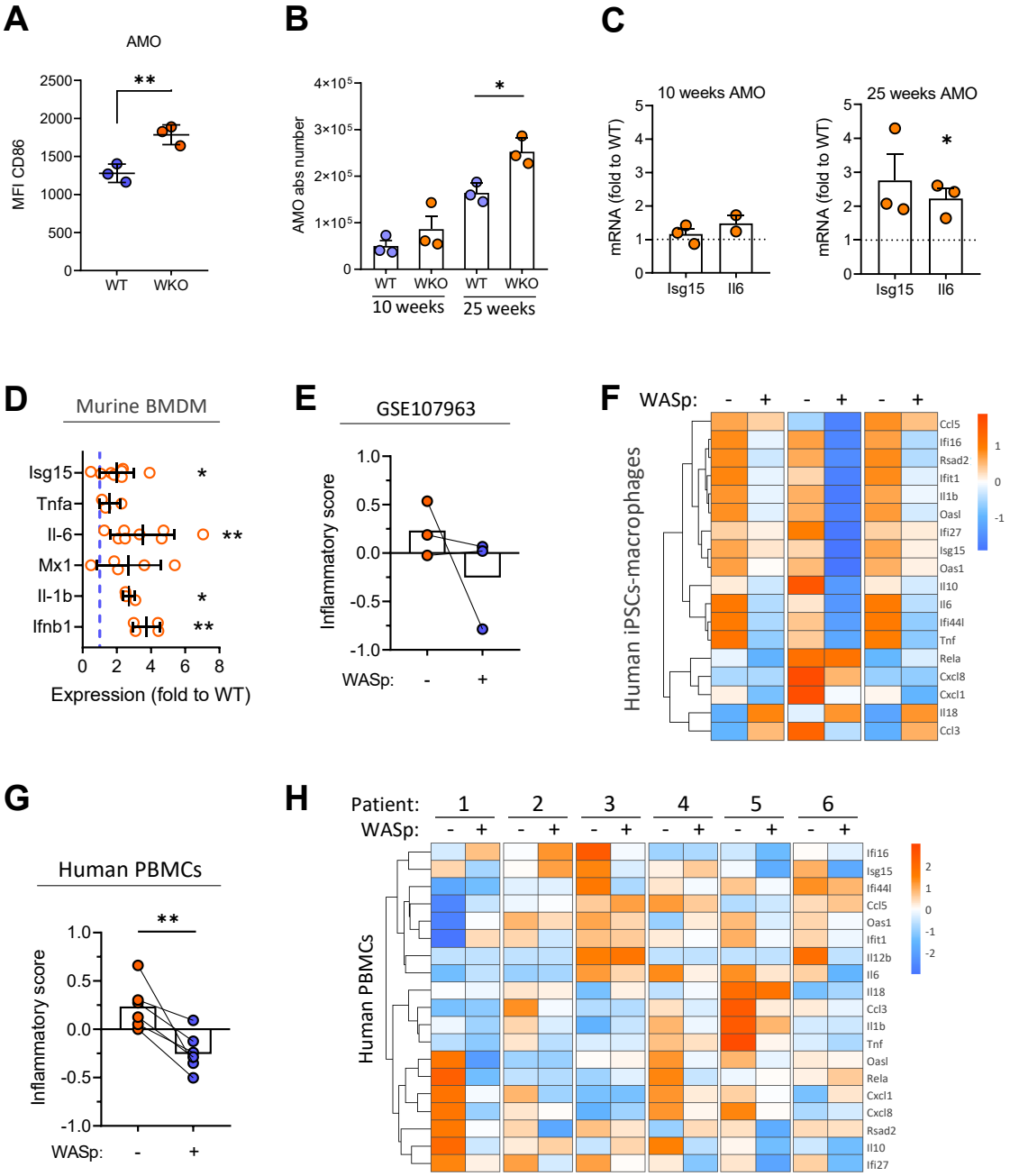
A
AMO
MFI CD86
2500
2000
1500
1000
500
0
**
WT
WKO
B
AMO abs number
4×10⁵
3×10⁵
2×10⁵
1×10⁵
0
*
WT
WKO
WT
WKO
10 weeks
25 weeks
C
10 weeks AMO
25 weeks AMO
mRNA (fold to WT)
Isg15
Il6
*
D
Murine BMDM
Isg15
Tnfa
Il-6
Mx1
Il-1b
Ifnb1
*
**
*
**
0
2
4
6
8
Expression (fold to WT)
E
GSE107963
Inflammatory score
1.0
0.5
0.0
-0.5
-1.0
WASp:
-
+
F
WASp:
- + - + - +
Human iPSCs-macrophages
Ccl5
Ifi16
Rsad2
Ifit1
Il1b
Oasl
Ifi27
Isg15
Oas1
Il10
Il6
Ifi44l
Tnf
Rela
Cxcl8
Cxcl1
Il18
Ccl3
1
0
-1
G
Human PBMCs
Inflammatory score
1.0
0.5
0.0
-0.5
-1.0
**
WASp:
-
+
H
Patient:
1
2
3
4
5
6
WASp:
- + - + - + - + - + - +
Human PBMCs
Ifi16
Isg15
Ifi44l
Ccl5
Oas1
Ifit1
Il12b
Il6
Il18
Ccl3
Il1b
Tnf
Oasl
Rela
Cxcl1
Cxcl8
Rsad2
Il10
Ifi27
2
1
0
-1
-2

Suppl. Figure 1

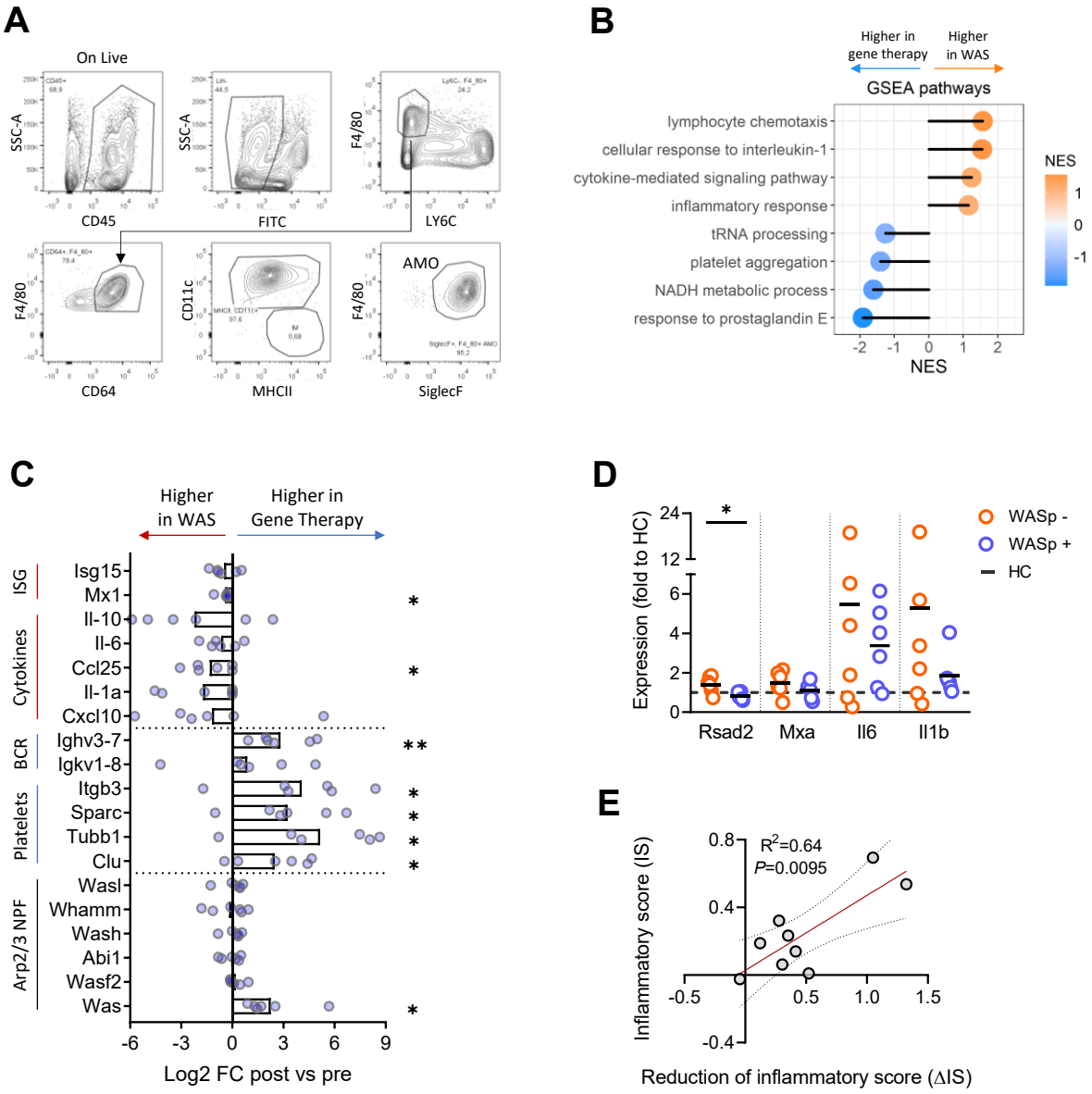

Figure 2

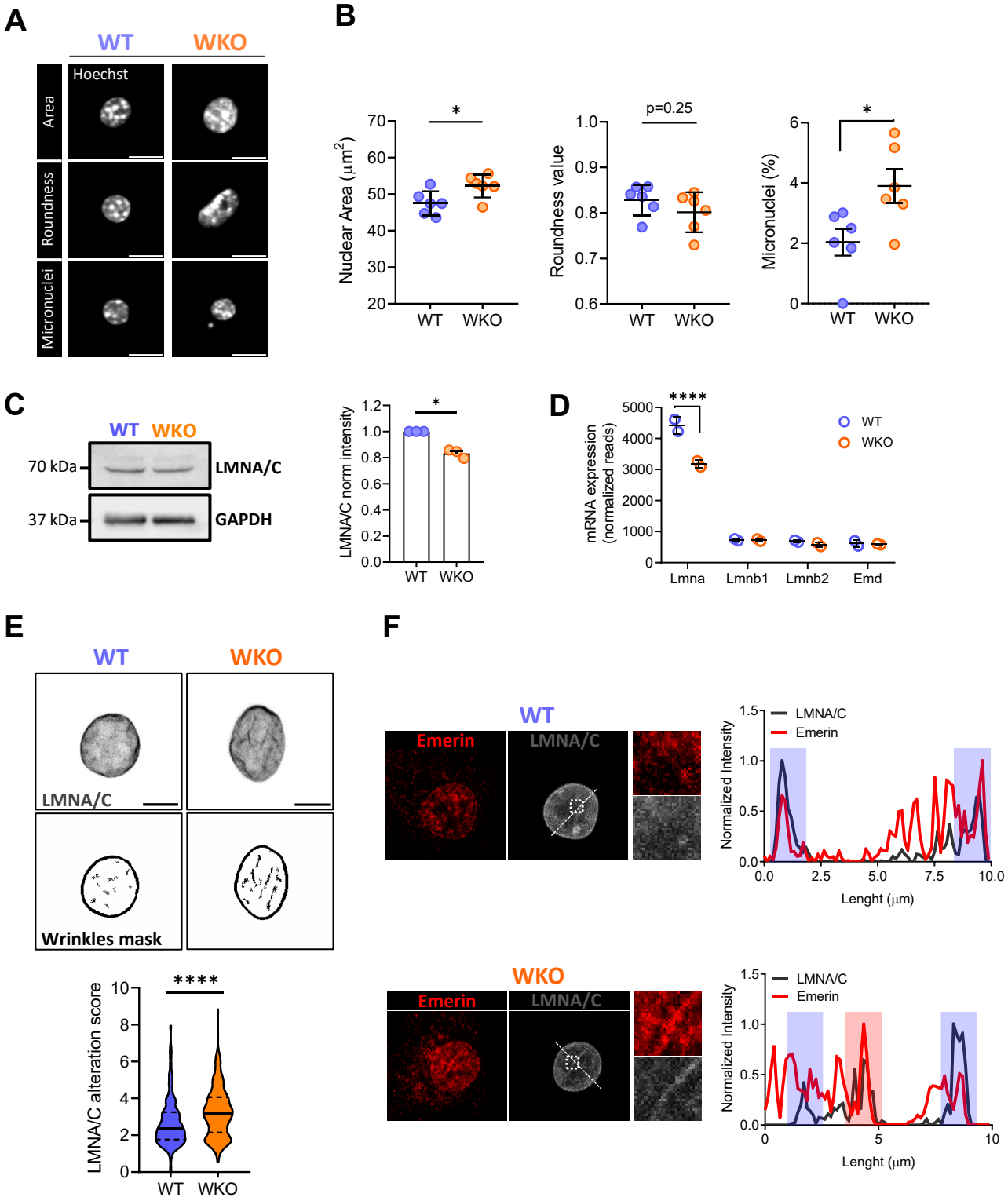
A
WT
WKO
Hoechst
Area
Roundness
Micronuclei
B
Nuclear Area (µm²)
Roundness value
Micronuclei (%)
p=0.25
WT
WKO
C
WT WKO
70 kDa
37 kDa
LMNA/C
GAPDH
LMNA/C norm intensity
D
mRNA expression (normalized reads)
WT
WKO
Lmna
Lmnb1
Lmnb2
Emd
E
WT
WKO
LMNA/C
Wrinkles mask
LMNA/C alteration score
F
WT
WKO
Emerin
LMNA/C
Normalized Intensity
Lenght (µm)

Suppl. Figure 2

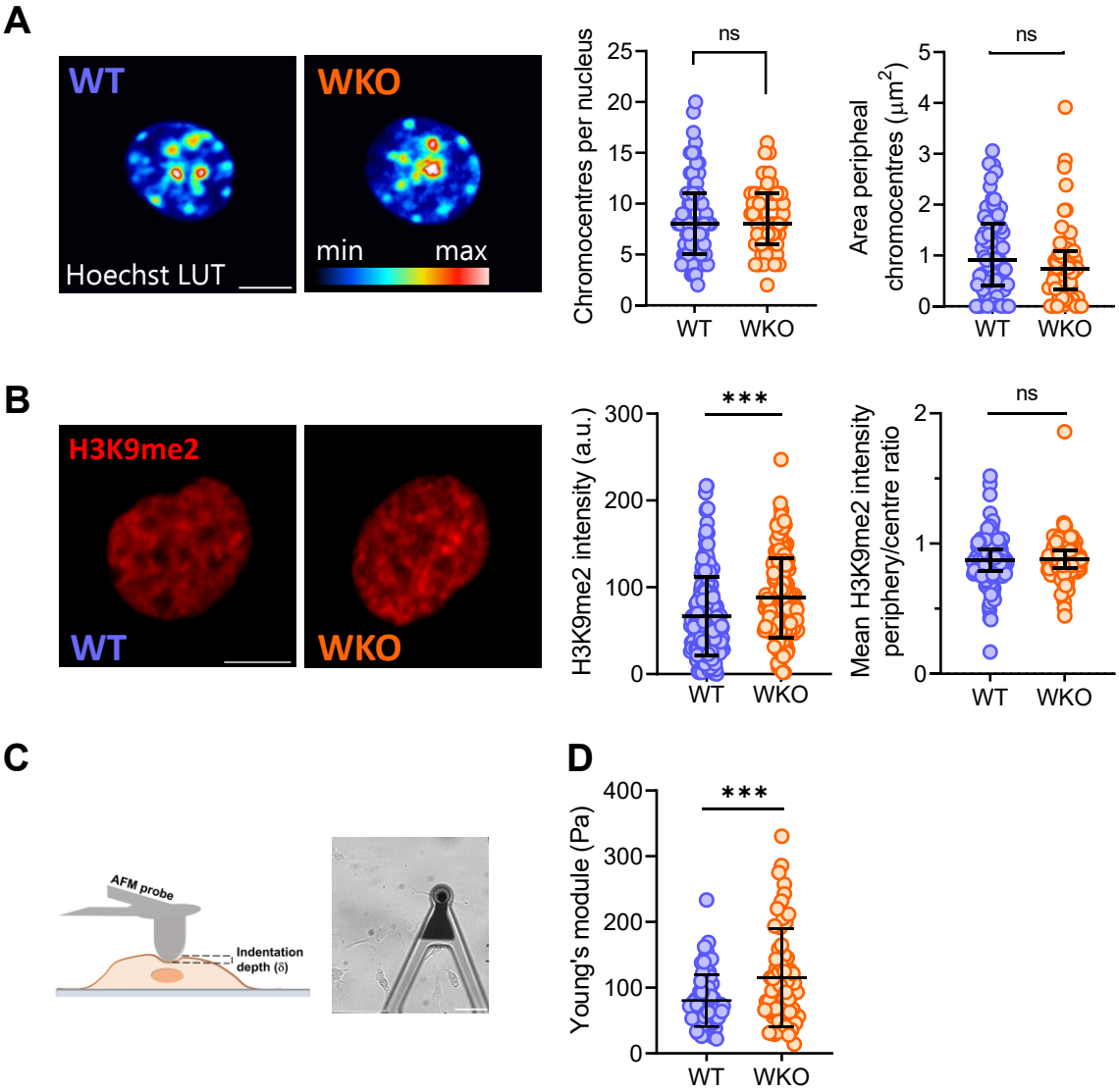

Figure 3

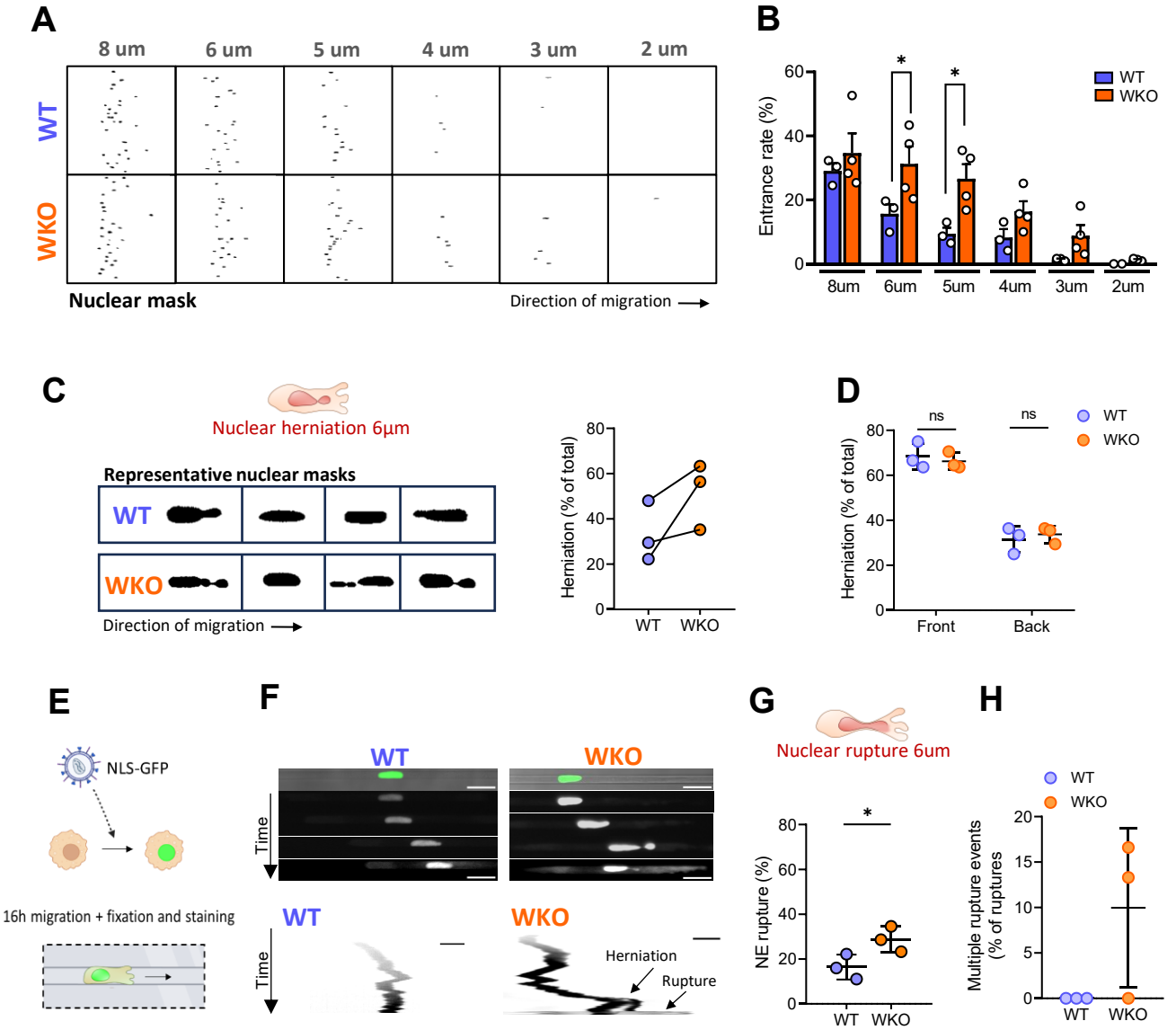
A
8 um
6 um
5 um
4 um
3 um
2 um
WT
WKO
Nuclear mask
Direction of migration
B
Entrance rate (%)
WT
WKO
8um
6um
5um
4um
3um
2um
C
Nuclear herniation 6µm
Representative nuclear masks
WT
WKO
Direction of migration
Herniation (% of total)
WT
WKO
D
Herniation (% of total)
ns
ns
WT
WKO
Front
Back
E
NLS-GFP
16h migration + fixation and staining
F
WT
WKO
Time
Herniation
Rupture
G
Nuclear rupture 6um
NE rupture (%)
WT
WKO
H
Multiple rupture events (% of ruptures)
WT
WKO

Suppl. Figure 3

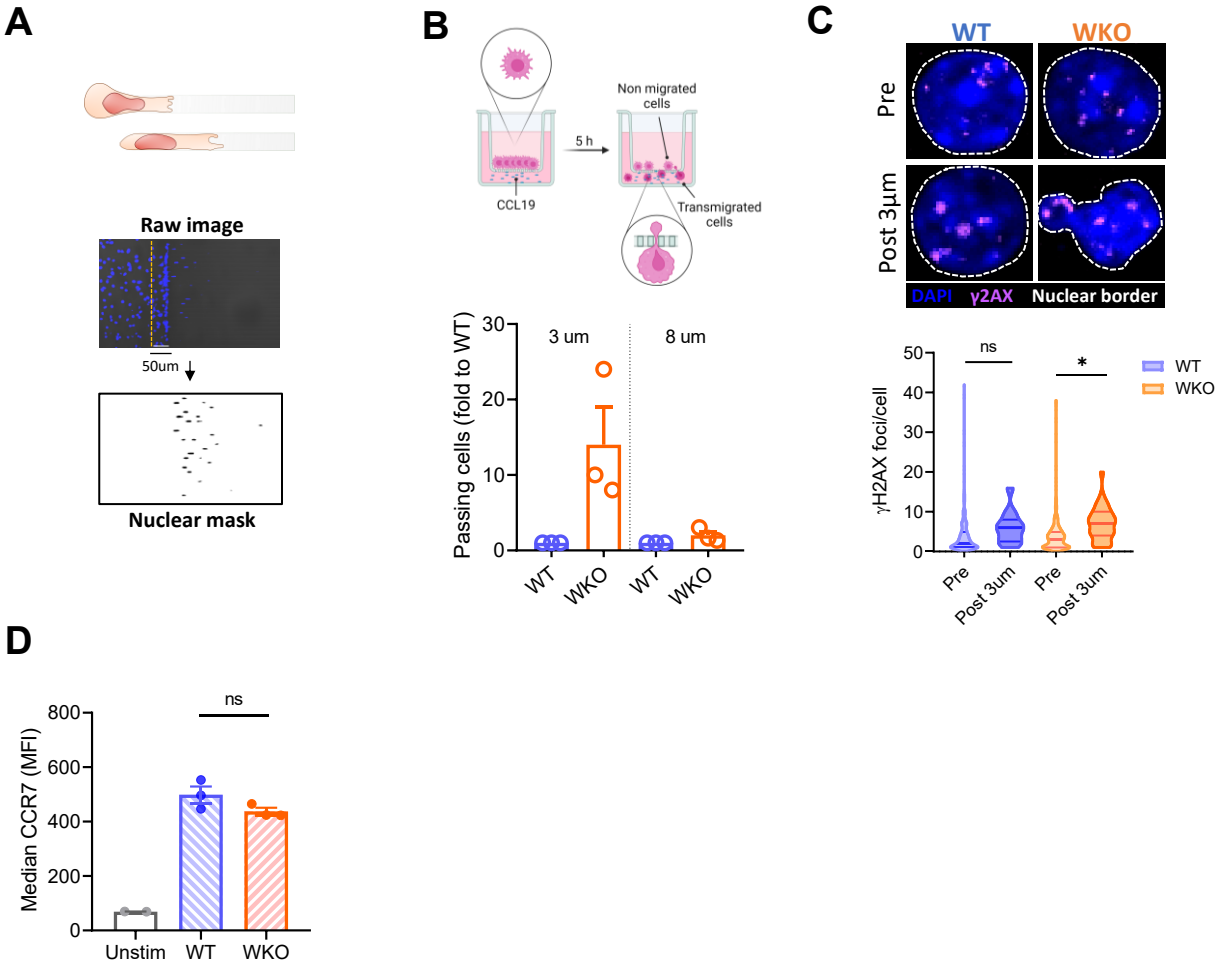

Figure 4

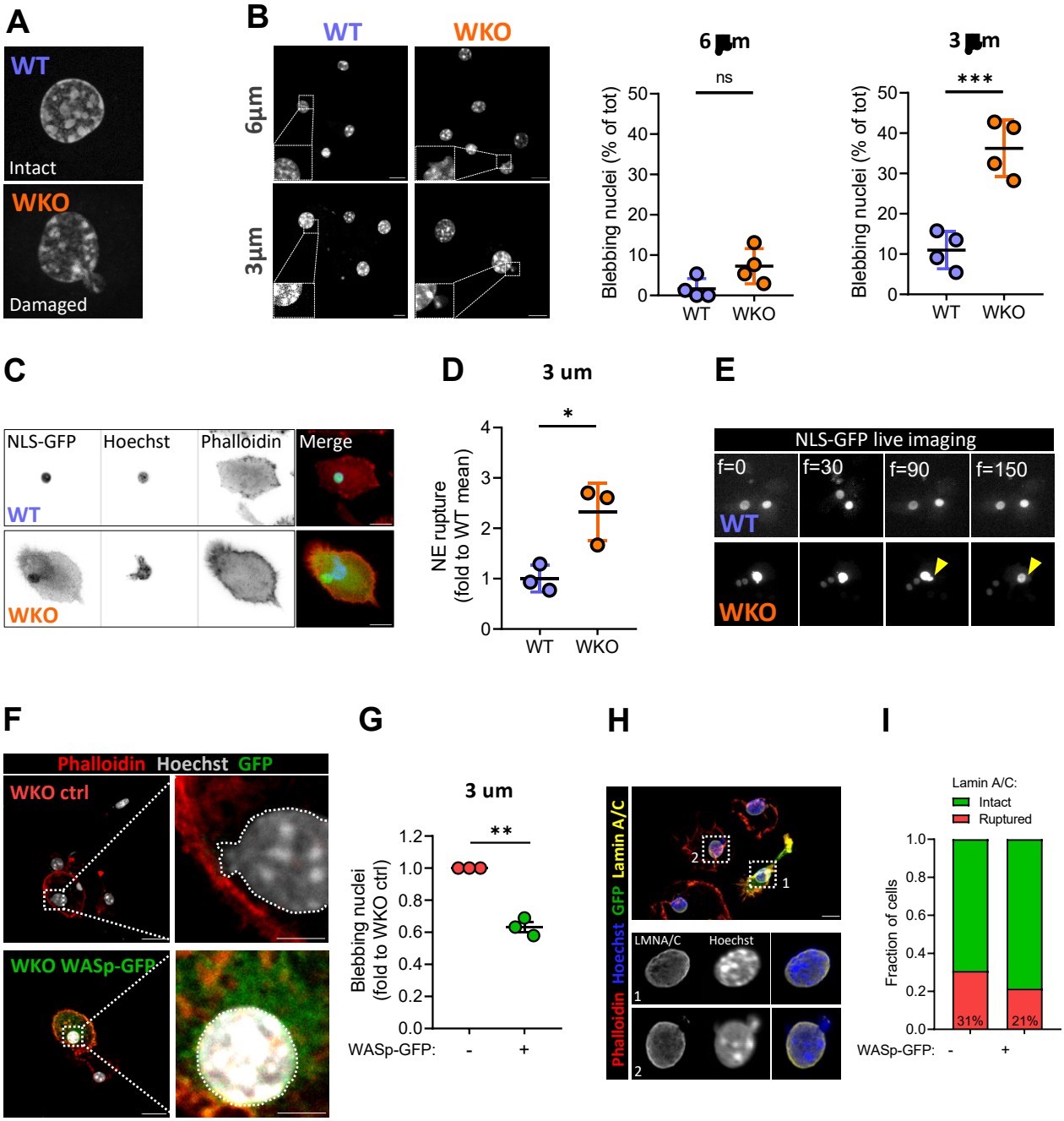
A
WT
Intact
WKO
Damaged
B
WT
WKO
6µm
3µm
6 µm
ns
Blebbing nuclei (% of tot)
WT
WKO
3 µm
***
C
NLS-GFP
Hoechst
Phalloidin
Merge
WT
WKO
D
3 um
*
NE rupture
(fold to WT mean)
WT
WKO
E
NLS-GFP live imaging
f=0
f=30
f=90
f=150
WT
WKO
F
Phalloidin Hoechst GFP
WKO ctrl
WKO WASp-GFP
G
3 um
**
Blebbing nuclei
(fold to WKO ctrl)
WASp-GFP:
-
+
H
Phalloidin Hoechst GFP Lamin A/C
LMNA/C
Hoechst
1
2
I
Lamin A/C:
Intact
Ruptured
Fraction of cells
31%
21%
WASp-GFP:
-
+

Suppl. Figure 4

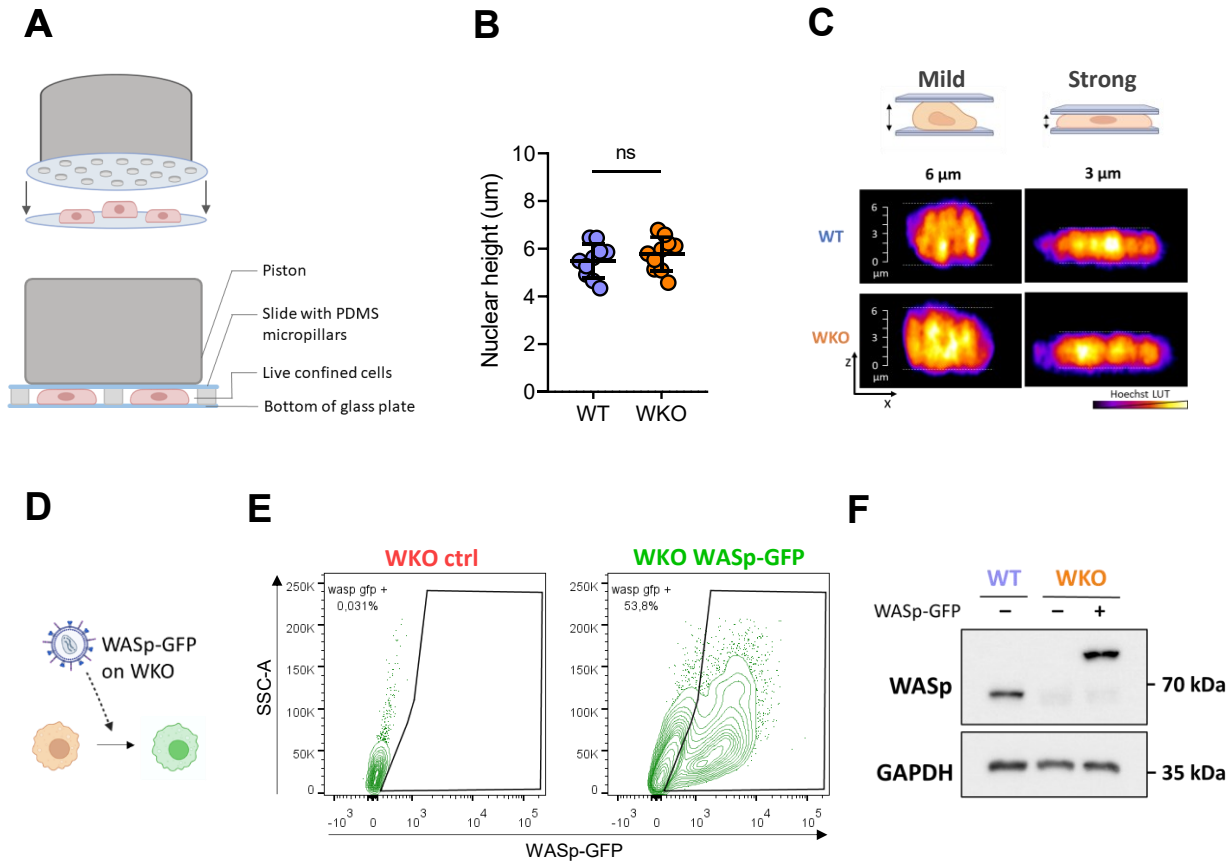

Figure 5

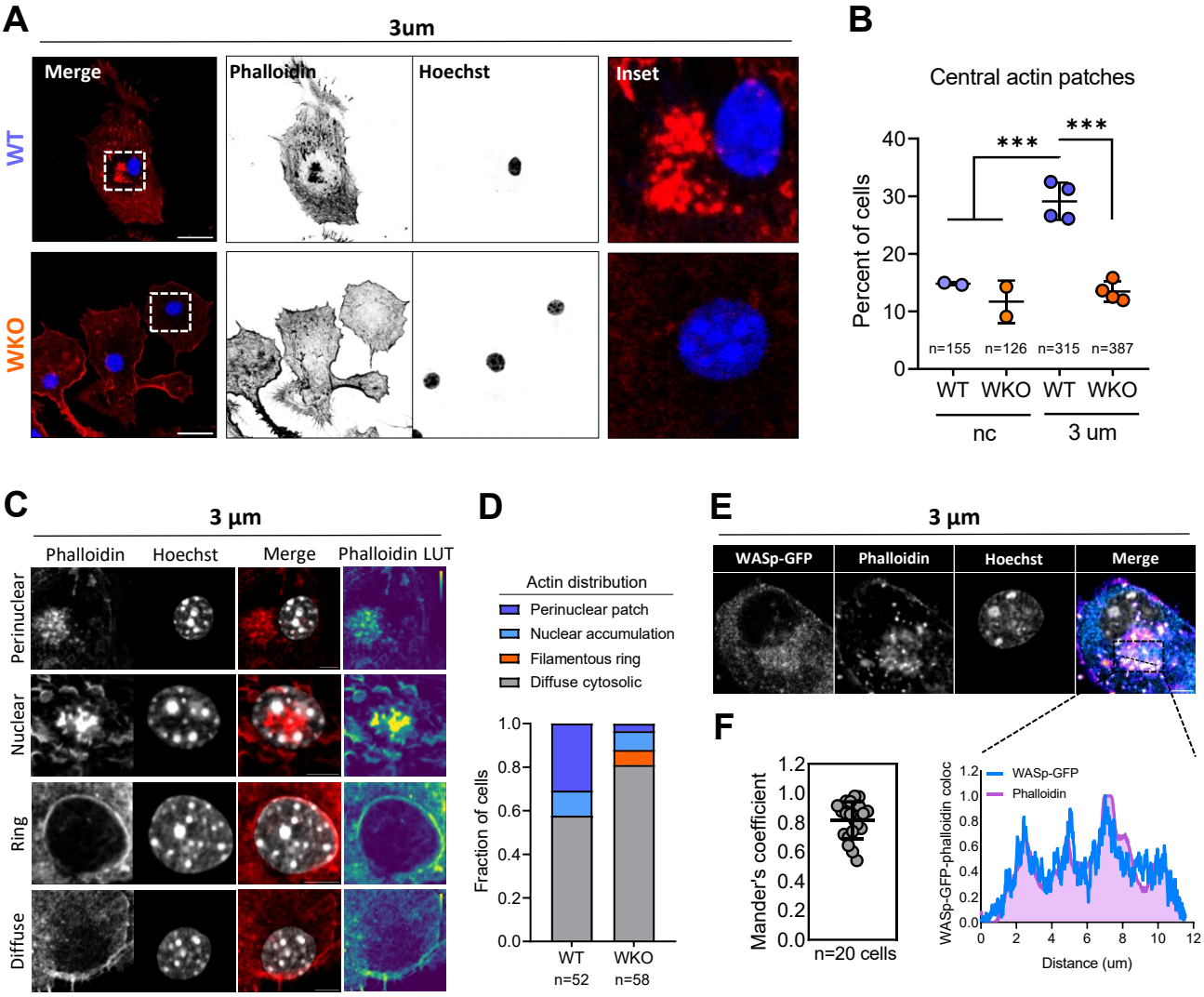
A
3um
Merge
Phalloidin
Hoechst
Inset
WT
WKO
B
Central actin patches
Percent of cells
***
***
n=155
n=126
n=315
n=387
WT
WKO
WT
WKO
nc
3 um
C
3 µm
Phalloidin
Hoechst
Merge
Phalloidin LUT
Perinuclear
Nuclear
Ring
Diffuse
D
Actin distribution
Perinuclear patch
Nuclear accumulation
Filamentous ring
Diffuse cytosolic
Fraction of cells
WT
n=52
WKO
n=58
E
3 µm
WASp-GFP
Phalloidin
Hoechst
Merge
F
Mander's coefficient
n=20 cells
WASp-GFP-phalloidin coloc
WASp-GFP
Phalloidin
Distance (um)

Suppl. Figure 5

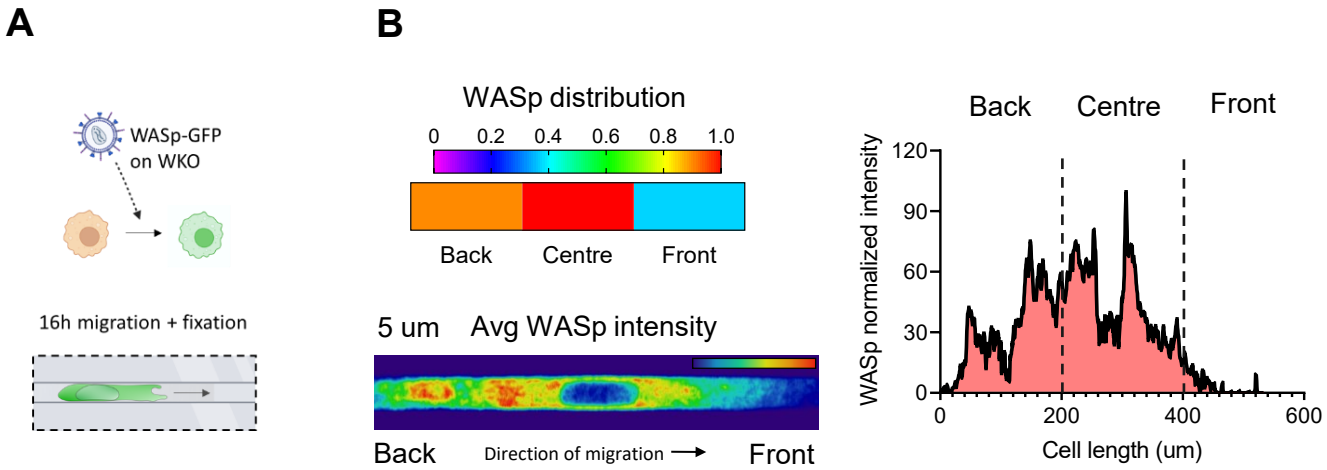

Figure 6

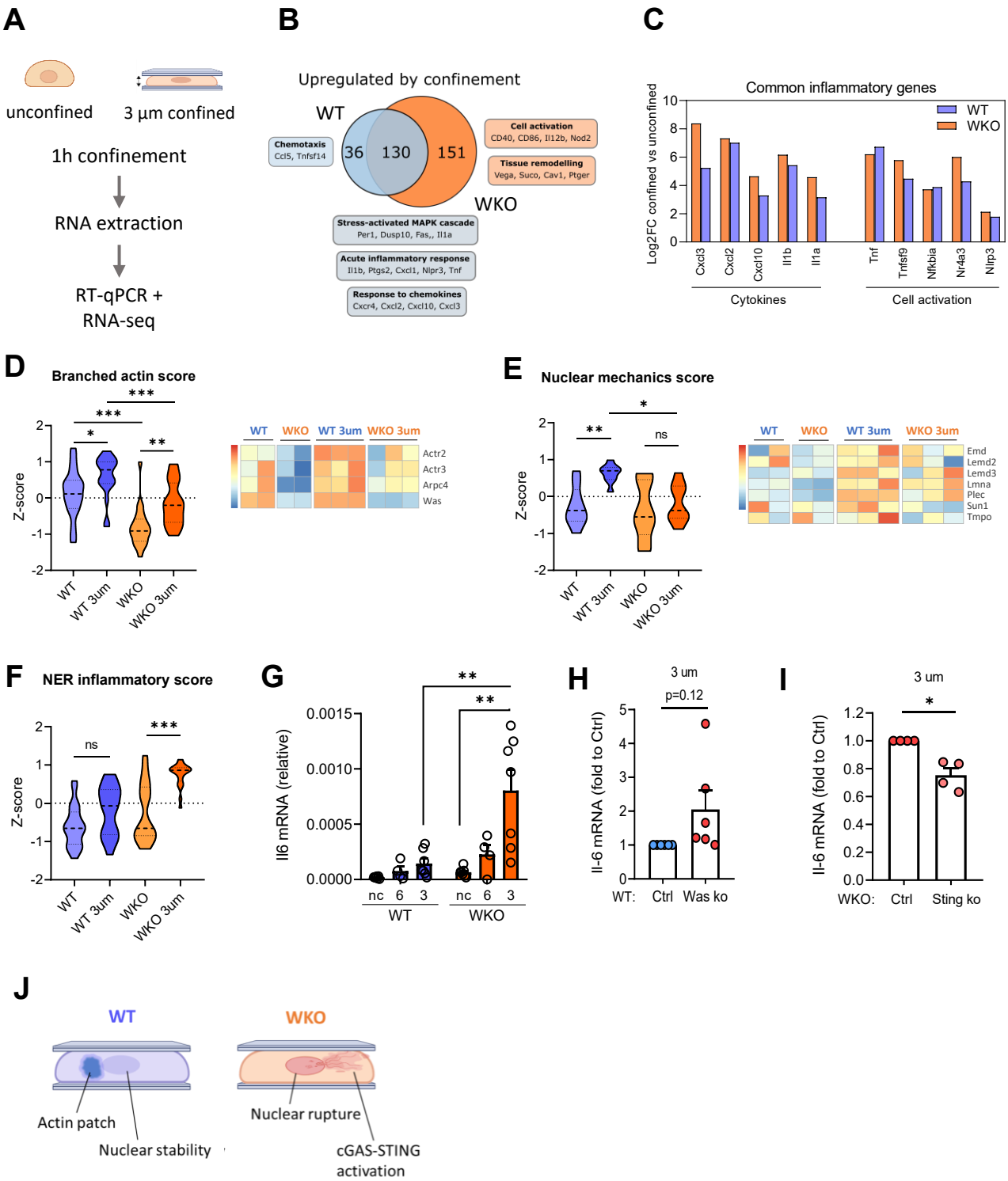
A
unconfined
3 µm confined
1h confinement
RNA extraction
RT-qPCR +
RNA-seq
B
Upregulated by confinement
WT
WKO
36
130
151
Chemotaxis
Ccl5, Tnfsf14
Cell activation
CD40, CD86, Il12b, Nod2
Tissue remodelling
Vega, Suco, Cav1, Ptger
Stress-activated MAPK cascade
Per1, Dusp10, Fas,, Il1a
Acute inflammatory response
Il1b, Ptgs2, Cxcl1, Nlpr3, Tnf
Response to chemokines
Cxcr4, Cxcl2, Cxcl10, Cxcl3
C
Common inflammatory genes
Log2FC confined vs unconfined
WT
WKO
Cxcl3
Cxcl2
Cxcl10
Il1b
Il1a
Tnf
Tnfsf9
Nfkbia
Nr4a3
Nlrp3
Cytokines
Cell activation
D
Branched actin score
Z-score
WT
WT 3um
WKO
WKO 3um
Actr2
Actr3
Arpc4
Was
E
Nuclear mechanics score
Emd
Lemd2
Lemd3
Lmna
Plec
Sun1
Tmpo
F
NER inflammatory score
ns
G
Il6 mRNA (relative)
nc
6
3
H
3 um
p=0.12
Il-6 mRNA (fold to Ctrl)
WT:
Ctrl
Was ko
I
WKO:
Sting ko
J
Actin patch
Nuclear stability
Nuclear rupture
cGAS-STING
activation
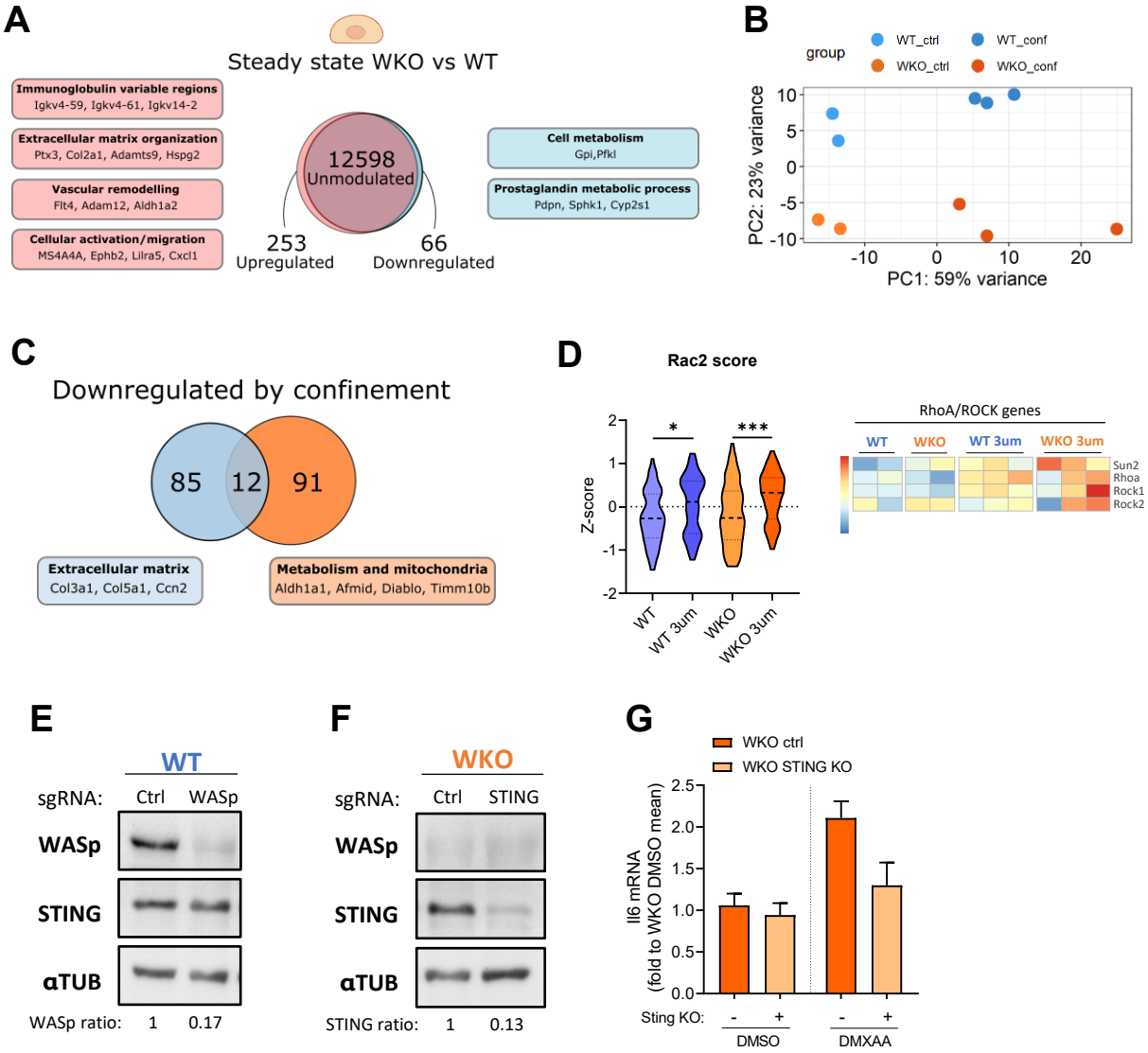
Suppl. Figure 6